# A Cautionary Tale: examples of the mis-location of small earthquakes beneath the Tibetan plateau by routine approaches

Timothy J. Craig
COMET, School of Earth and Environment, The University of Leeds, Leeds, United Kingdom. LS2 9JT
t.j.craig@leeds.ac.uk

James Jackson, Keith Priestley
Department of Earth Sciences, University of Cambridge, Cambridge, CB3 0EZ, UK.

Göran Ekström
Lamont-Doherty Earth Observatory of Columbia University, 61 Route 9W, Palisades, NY 10964, USA

January 19, 2023

**Abstract**

Earthquake moment tensors and centroid locations in the catalogue of the Global CMT (gCMT) project, formerly the Harvard CMT project, have become an essential resource for studying active global tectonics, used by many solid-Earth researchers. The catalogue's quality, long duration (1976–present), ease of access and global coverage of earthquakes larger than about Mw 5.5 has transformed our ability to study regional patterns of earthquake locations and focal mechanisms. It also allows researchers to easily identify earthquakes with anomalous mechanisms and depths that stand out from the global or regional patterns, some of which require us to look more closely at accepted interpretations of geodynamics, tectonics or rheology. But, as in all catalogues that are, to some extent and necessarily, produced in a semi-routine fashion, the catalogue may contain anomalies that are in fact errors.

Thus, before re-assessing geodynamic, tectonic or rheological understanding on the basis of anomalous earthquake locations or mechanisms in the gCMT catalogue, it is first prudent to check those anomalies are real. The purpose of this paper is to illustrate that necessity in the eastern Himalayas and SE Tibet, where two earthquakes that would otherwise require a radical revision of current geodynamic understanding are shown, in fact, to have gCMT depths (and, in one case, also focal mechanism) that are incorrect.

**Keywords:** Earthquake catalogues, seismology, earthquake locations

# 1 Introduction

Earthquakes provide the most immediate and accessible evidence for tectonic activity on Earth. Their locations and fault-plane solutions were central to the discovery and acceptance of Plate Tectonics in the oceans (e.g., Isacks et al, 1968), and their depth distribution has long formed an observational basis for believing in a temperature-dependence of strength in the lithosphere (e.g., Chen and Molnar, 1983). On the continents, where active deformation is generally more distributed than in the oceans, earthquake focal mechanisms were again central to revealing the more complicated and diverse tectonic patterns and processes that occur (e.g., McKenzie, 1972; Molnar and Tapponnier, 1975). To this day, seismologically-determined locations and focal mechanisms of earthquakes remain essential datasets, supplemented now by geodetic observations, that underpin fields ranging from regional continental tectonics and geodynamics to seismic hazard assessment.

Although it has been possible to construct reliable fault-plane solutions for earthquakes anywhere that are larger than about M6 since the installation of the WWSSN (World-Wide Standardized Seismograph Network) in the early 1960s, the situation improved dramatically in the late 1970s with the advent of digital seismograms, synthetic seismogram routines, and computational capacity that allowed inversion of waveforms for earthquake source parameters. In particular, the Global Centroid Moment Tensor (gCMT; Ekström et al, 2012) project (formerly the Harvard Centroid Moment Tensor project; Dziewonski et al, 1981; Dziewonski and Woodhouse, 1983; Ekstrom et al, 1998) has been a widely-used catalogue for global earthquake source parameters. Covering earthquakes from 1976 onwards, it has routinely provided, quickly, openly and on-line, high-quality source parameters world-wide for almost all earthquakes larger than about $M_w$ 5.2 and, with the steadily improving number and distribution of global seismic stations, now often provides solutions for earthquakes as small as about $M_w$ 4.7, commonly disseminated to the global community through the website `www.globalcmt.org`. The transformation provided by this resource can hardly be overstated: prior to 1976, earthquake focal mechanisms were usually determined from first-motion polarities of $P$ waves read on WWSSN film chips or microfilms, a process that generally took an experienced researcher a day for each earthquake, producing a result that was often far less well constrained than one based on the inversion of body waves. Unlike waveform inversion procedures, that process produced no constraint on the earthquake depth, unless the depth-phase arrivals $pP$ and $sP$ were visibly separated from $P$, which is very rarely the case for crustal earthquakes, especially those large enough to be detected globally on WWSSN instruments.

Thus, not surprisingly, the gCMT catalogue is usually the first resource used in studies where earthquake focal mechanisms and depths are of interest for active tectonics, geodynamics or rheology. Its time-span (about 45 years) and completeness (which varies both geographically and through time, but is probably global for $M_w \geq 5.5$) confirms tectonic patterns that were initially inferred from much sparser data, though it is remarkable how robust such early inferences often were. But the gCMT catalogue, like all almost-routinely produced datasets, and in spite of its general reliability and utility, is itself capable of harbouring anomalies and errors. Before attaching significance to particular anomalous events that it contains, it is important to check their accuracy, if possible by independent means. That is the purpose of this paper, in which we examine some small events in the gCMT catalogue in Tibet which, if correct, would require a radical re-assessment of our current understanding of continental tectonics, geodynamics and rheology. We show that their gCMT depths, and in one case also the focal mechanism, are in fact incorrect, and that no such re-assessment is necessary. We also assess how and why the gCMT analysis of these earthquakes went astray.

## 2 Anomalous earthquakes beneath the Himalayas and Tibet

Figure 1 shows focal mechanisms and centroid depths for well-constrained earthquakes (those verified by independent waveform-based modelling) in and around the Tibetan Plateau from the compilation of Craig et al (2020), along with the four events from the gCMT catalogue on which we focus here. Shallow (<20 km) seismicity is widespread, but deeper seismicity is confined to two main regions: the lower crust of peninsular India (down to $\sim$ 45 km), and at depth ($<$ 25 km) beneath southern and northwestern Tibet. The deeper (25 – 100 km) seismicity fits a simple pattern, with a strong and seismogenic Indian lower crust extending from peninsular India several hundred kilometres beneath Tibet, particularly at the eastern and western extremes of the Himalayas (see Craig et al (2020) for a summary). As the mid crust and, further north, lower crust, beneath the plateau become hotter, they progressively cease to be seismogenic, leading to a bifurcating pattern of seismicity, with widespread earthquakes in the uppermost crust, and a tongue of deeper seismicity following the Moho beneath southern Tibet, eventually pinching out beneath central Tibet, as the underthrust material becomes too hot to sustain brittle failure (Priestley et al, 2008; Craig et al, 2012, 2020). Across the Tibetan Plateau itself, shallower seismicity rarely extends below 12-15 km from the surface, leading to an aseismic mid crust, with no earthquakes between $\sim$ 20 km and $\sim$ 60 km. Earthquake focal mechanisms also show a simple pattern: thrust-faulting earthquakes are concentrated around the margins of the plateau at elevations $\lesssim$ 3500 m, particularly along the Himalayas (see Figure 1b), whilst within the high plateau at elevations $\gtrsim$ 3500 m, earthquakes show a mixture of strike-slip faulting and normal faulting.

We focus on four earthquakes in the eastern Himalayas and southeast Tibet, highlighted on Figure 1, and summarised in Table 1. The two most obvious anomalies are the events on 2003/2/11 and 2005/8/20.

The event on 2005/8/20 is anomalous both for its gCMT mechanism and centroid depth of 96 km. It is the only reverse-faulting solution in central Tibet, where shallow events otherwise follow the well-established pattern of normal- and strike-slip faulting in the higher ground (Figure 1b). Its gCMT centroid depth of 96 km is similar to that of a well-known population of deeper earthquakes (e.g., Monsalve et al, 2006; Craig et al, 2012; Schulte-Pelkum et al, 2019) in the SE and far NW of Tibet (shown on Figure 1a,c), which are thought to be in the Precambrian shield of India as it is under-thrust north beneath Tibet. Within such shields earthquakes are known to occur in anhydrous lower crust or even uppermost mantle, to temperatures of up to about 600 − 650°C, (e.g., J. Jackson, 2021) and in this case show that India reaches at least 300 km north beneath the Himalayan range front (Craig et al (2012); see Figure 1c). But if the gCMT catalogue depth for this event is correct, it suggests that India penetrates about 200 km north beyond that, while (by implication) remaining colder than about 600°C . That would be interesting in itself, because the rigidity of underthrusting India is likely to control the deformation within the gravity current of the mid-Tibetan crust that flows over it (Copley et al, 2011), and also because its known presence and temperature would put a useful constraint on thermal models of the Tibetan crust (e.g. Bollinger et al, 2006; Craig et al, 2012; McKenzie et al, 2019b; Craig et al, 2020). We show later that this event was in fact a normal-faulting earthquake at about 4-6 km depth (see Section 4.1).

The event on 2003/2/11 is unusual for its gCMT centroid depth of 46 km (Figure 1b), putting it in the middle of what is estimated to be the hottest part of the thick Tibetan crust, based on temperature calculations that account for radiogenic self-heating and age: an inference supported by low seismic velocities and high seismic attenuation (e.g. McKenzie et al, 2019b; Craig et al, 2020). Temperatures at that depth are expected to substantially exceed 600°C , and this earthquake depth, if correct, would require a reassessment of our notions regarding the temperature control of seismicity and also geotherm calculations, as earthquakes in Phanerozoic crust are usually restricted to less than about 350°C (e.g., Chen and Molnar, 1983). All other earthquakes with body-wave derived depths nearby are shallower than 10–15 km, as expected (e.g., Langin et al, 2003;

Liang et al, 2008; Craig et al, 2012). We show later that the correct depth is about 5–7 km.

The 2008/6/19 event is of note only because its gCMT centroid depth of 18 km would be unusually deep for any region dominated by normal faulting that is outside a Precambrian shield (e.g., Craig and Jackson, 2021). In this area of Tibet all well-constrained depths are shallower than 12 km (Figure 1c) and the effective elastic thickness is less than 4 km (McKenzie et al, 2019b); both of which are consistent with the expected high temperatures in the mid crust (see above, the 2003/2/11 event). We show later that the correct depth is about 6 km, and this is no real surprise: the routine gCMT procedures and algorithms are not expected to provide a depth resolution better than about 10-15 km for shallow earthquakes (Engdahl et al, 2006), and this event is included here just to make that point.

Generally, the gCMT depth resolution does improve markedly for earthquakes deeper than about 20–30 km, particularly for more recent events with better data coverage, and most of the depths it reports greater than $\sim$30 km are approximately correct. To show this, we examine an event on 2005/3/26, whose gCMT depth (70 km) and focal mechanism are both approximately correct, showing the event to be one of the well-established pattern of deep earthquakes within the Indian shield beneath SE Tibet (Figure 1a,c). There was therefore no *a priori* reason to discount the gCMT depth for the event of 2005/8/20, apparently at 96 km; although as we shall show it is, in fact, incorrect (see Section 4.3).

Table 1 lists the source parameters for all four events, determined by different methods or agencies. Locations from the NEIC and ISC-EHB are hypocentres, determined by phase-arrival times; those from CMT algorithms (either gCMT or our regional inversions) are centroids. The centroid is, in principle, the weighted centre of seismic moment within a finite source area; but since the expected dimension of faulting in all four earthquakes is smaller than about $3 \times 3$ km$^2$, the difference between the position of the hypocentre (rupture initiation) and centroid is unimportant here, and well within any likely errors. The CMT algorithms generally solve for the 6 independent elements of the seismic moment tensor, with the constraint that the diagonal elements sum to zero (i.e., no volume change).

Table 1 displays the 'best-double-couple' solutions, in which the eigenvalue with the smallest absolute value is set to zero, while maintaining the orientation of the three eigenvector axes. The extent to which that smallest eigenvalue is actually close to zero is shown by the percentage double-couple ($\gamma$; defined below). Only the event on 2008/6/19 has an apparently significant non-double-couple component in the gCMT solution. Real non-double-couple components do occur for extremely shallow (<1 km) events associated with volcanic processes (e.g., Shuler et al, 2013), and at more substantial depths for genuinely complicated ruptures on systems of faults with different orientations, whose individual double-couples sum to a non-double-couple total moment tensor (e.g., Wei et al, 2013; Ruppert et al, 2018). But they can also arise from noise in the seismograms, especially for small earthquakes like the 2008/6/19 event. We do not believe that any of these events involved anything substantial other than faulting on a simple planar surface, so focus on the best-double-couple mechanisms.

In the following sections, we outline our data analysis approach (Section 3), and then consider each of these earthquakes in detail (Section 4). In Section 6, we then assess where the gCMT approach erred in its original assessment of these events, and the implications this may have.

# 3 Methods

We employ four seismological approaches in re-evaluating the depths and mechanisms of these four earthquakes. Each draws on different data, in terms of epicentral distances and frequency contents used, and offer independent constraints on the source parameters, particularly depth, of these earthquakes. All use higher frequencies than included in gCMT inversions, and are aimed at studying signals from smaller-magnitude earthquakes, where low-frequency energy is usually lacking.

In Section 6.1, we employ the modern gCMT processing approach to reanalyse the four earthquakes studied here. This differs from the gCMT approach used at the time of occurrence of these earthquakes, as detailed in Ekström et al (2012).

## 3.1 Regional waveform inversion

We first employ regional waveform inversion to determine the source mechanism, moment, and location (including depth) of each of the four earthquakes studied. We use the approach of Heimann et al (2018) to invert three component waveforms (vertical, radial, and tangential) from seismometers within 1000 km of the reported earthquake location (station distributions for each earthquake are shown in Supplementary Material). Green's functions are calculated using the approach of (Wang, 1999) for a layered visco-elastic halfspace, and velocity structures in each case are determined based on the closest available profile from CRUST2 (Bassin et al (2000) and subsequent updates - see Section 5 for sensitivity tests on the velocity structure). Waveforms are filtered between 0.03 and 0.09 Hz ($\sim 11 - 33$ second periods), and a time window encompassing local and regional $P$, $S$ wave arrivals, their related regional depth phases, and the surface wave arrivals is used in our inversion. The approach of Heimann et al (2018) undertakes a Bayesian inversion, producing probability distributions for each parameter. In each case, we invert for a 6-component deviatoric moment tensor, location, depth (constrained to lie between 1 and 100 km), and source duration ($1 - 5$ seconds, consistent with expected rupture duration for the magnitudes of earthquake considered). Station locations relative to the earthquake source (azimuth and distance) are recalculated for each trial source location, and Green's functions re-selected from a pre-calculated array calculated at 1 km intervals in depth and distance. Waveforms are re-aligned by cross-correlation for each trial model.

In Figure 2 we show the probability density functions (hereafter referred to as PDFs) for depth for each of our four study earthquakes. In Figures 4, 5, 6 and 7 we show waveform fits for selected stations for the overall best-fit model and a range of fixed depths, illustrating how and where the details of the waveform allow us to discriminate between different depths and mechanisms.

To discriminate between different candidate source depths it is important to model accurately the amplitudes of both the initial family of $P$-wave arrivals ($Pg$, $Pn$, $PmP$, etc), and the subsequent family of $S$-wave arrivals ($Sg$, $Sn$, $SmS$, $Lg$, etc), including the emerging surface wave train. At the frequency range and epicentral distance used in our regional inversion, both of these groups of phases coalesce into two complex wavepackets. Of these two groups of phases, the first set is typically visible only on the vertical and radial components, whilst the second is visible on all three components (see Figure 7 and 4 for examples). The amplitude of the second set of arrivals is particularly depth-dependent, decreasing sharply with increasing depth, with the reduced amplitude of the the surface wave train. As we shall show, the disappearance of a dominant $S$-wave family arrival at greater depth often allows, in the case where an event is really shallow, for inversion to model internal sections of the waveform for deeper events with the $P$-wave phase group only, leading to an apparent good fit to a small section of the waveform (for a radically different source mechanism), but failing to fit the earlier and later sections of the waveform. This allows inversion approaches to settle on a stable local misfit minima, and, in many cases, this leads to a switch in the best fit mechanism as a function of depth, in order to fit the polarity of the $S$-wave family using the synthetic $P$-wave group.

To help in assessing the moment tensors from various sources, we define two metrics. For each moment tensor, we follow Jackson et al (2002) in calculating the percentage double couple, $\gamma$:

$$\gamma = 100 \times \left(1 - \frac{3 \times |\lambda_2|}{|\lambda_1| + |\lambda_3|}\right) \qquad (1)$$

where $\lambda_n$ is the $n^{th}$ eigenvalue of $\mathbf{M}$, the moment tensor. This $\gamma$ value shows the degree to which the moment tensor can be represented accurately by a simple double couple, with no deviatoric component. $\gamma$ is defined from the absolute value of the intermediate eigenvalue (2) relative to the average of the other two, (1,3) normalized so that a pure double-couple source (with eigenvalues -1,0,+1) is 100%, while a linear vector dipole (e.g. -0.5,-0.5,+1.0) is 0%. Under the assumption that earthquakes at magnitude $M_w \sim 5$ are hosted on faults, and rupture only a single planar segment of such faults with relatively little complexity, we therefore expect $\gamma$ to be close to 100% in cases where the source is accurately characterised. Inaccurate characterisation of the moment tensor, feeding in to a low $\gamma$ value, would be the result of either a poor fit between synthetics and the observed data, implying a poorly-constrained source mechanism, poor azimuthal coverage, resulting in an underconstrained source mechanism, or a small signal-to-noise ratio in the data, resulting in the mapping of noise into the source mechanism.

To aid with assessing the similarity between the moments tensors derived from the gCMT inversion and from our regional waveform inversion, we follow Sandiford et al (2020) in determining a similarity index ($\chi$) between the global (gCMT) and regional (rCMT) moment tensors. We define this similarity as:

$$\chi = \frac{\mathbf{M}_{ij}^{\mathrm{gCMT}} : \mathbf{M}_{ij}^{\mathrm{rCMT}}}{||\mathbf{M}^{\mathrm{gCMT}}||\,||\mathbf{M}^{\mathrm{rCMT}}||} \qquad (2)$$

where $||\mathbf{M}||$ is the norm of the moment tensor $\mathbf{M}$, and : is the tensor double dot product. Identical moment tensors would yield a $\chi$ of 1, with decreasing $\chi$ indicating decreasing similarity. Broadly speaking, studies in subduction zones suggest that observational uncertainty typically allows for variability between 1 and 0.75 between seismological moment tensors and known fault orientations (Sandiford et al, 2020; Craig et al, 2022).

Under the assumption that earthquakes of the magnitude studied here are unlikely to be anything other than slip on a small planar surface, and should therefore not contain significant non-double couple components, we also run an inversion for each earthquake where the mechanism is constrained to be a pure double couple ($\gamma = 100$), and with all other parameters free, to test the impact that incorporating non-couple elements into the moment tensor may have on all source parameters (tan-shaded rows on Figures 4, 5, 6, 7).

Full results from our regional centroid moment tensor inversions are given in Table 1.

## 3.2 Surface wave amplitudes

We also conduct more detailed analysis of the fundamental-mode surface-wave amplitudes generated by our four earthquakes, observed at far-regional distance ($10^\circ$ – $20^\circ$

epicentral distance). Surface-wave excitation of the fundamental mode is highly dependent on earthquake source depth, particularly for smaller earthquakes like those in the magnitude range we consider. $M_w \sim 5$ earthquakes with shallow source depths can still generate substantial surface waves, with amplitudes at far-regional distances significantly greater than the observed body-wave amplitudes, but as source depth increases into the mid and lower crust, surface wave amplitudes decrease. Therefore, if the reported lower-crustal/upper-mantle depth of some of these earthquakes is correct, we would expect quite small amplitude surface waves at such distances, whereas if they are, in fact, upper crustal, substantially larger surface waves will be expect.

To assess this, we select stations at far-regional distances, take the vertical component (therefore focusing on Rayleigh waves), and filter using a Butterworth bandpass centred on 0.05 Hz. We then correct the amplitudes for geometrical spreading, and normalise to 1000 km epicentral distance and the moment of the largest of our study earthquakes (2003/2/11). In Figure 9, we show waveforms for all four earthquakes observed at the broadband station II.AAK (observing distance between 1752 and 2033 km for our events). In supplementary material we show similar plots for three other stations (IC.QIZ, IC.WMQ, IC.XAN) at different azimuths.

## 3.3 Teleseismic array processing

In the third approach, we draw on data from small-aperture seismic arrays at teleseismic distances, to search for the presence or absence of depth phases – near-source surface reflections, which arrive shortly after the direct $P$-wave arrival. When detected, these can be used to precisely determine the earthquake source depth. We use data from arrays in Canada (Yellowknife array), the USA (ILAR array), Germany (GERESS array), and Australia (Alice Springs and Warramunga arrays). Each of these arrays has an aperture of only a few km, with the intention that short period signals (e.g. 1-4 Hz) are coherent between sensors and that the signal-to-noise ratio of coherent arrivals can be improved by delay-and-stack beamforming (e.g., Rost and Thomas, 2002). Similarly, estimating the coherence or relative power of beams in different directions allows us to estimate the backazimuth and apparent velocity of incoming wavefronts. This assists in confirming arrival detection, and helps to build confidence that a given signal is indeed associated with our event of interest, on the basis of directional coherence of arrivals. We show the results from this analysis for two events on 2005/8/20 and 2008/6/19, in Figures 3 and 8 respectively. Note that this approach offers an independent approach to determining the depth, but offers no constraint on the focal mechanism.

### 3.4 Teleseismic broadband instruments

Finally, we draw on data from available broadband seismometers at teleseismic distances. Whilst the earthquakes studied here are too small for a detectable signal to be easily or commonly observed, on rare occasions for seismometers in particularly well-sited, noise-free locations, the direct $P$ wave and its depth phases are observable in single-station data. We show filtered waveforms (0.5 – 2.0 $Hz$) for a small number of selected stations were these phases are observable, to supplement the results from the small-aperture arrays. We also use synthetic seismograms, calculated using the WKBJ routines of Chapman (1978); Chapman et al (1988) to test candidate depths against observed broadband waveforms (see Figure 3). Synthetics are calculated in each case using a simple impulsive source-time function, and our revised moment tensor from regional waveform inversion.

## 4 Earthquake results

### 4.1 The 2005/8/20 earthquake

This earthquake is anomalous in both its gCMT mechanism and its depth. It occurred on the $20^{th}$ August 2005, and was reported by the gCMT catalogue as having a moment tensor dominated by east-west striking thrust faulting, indicating north-south shortening, and with a location placing it deep beneath central Tibet, at a centroid depth of 96.3 km, well below estimates of the local Moho (Gilligan and Priestley, 2018). The NEIC and ISC-EHB also reported traveltime-based locations and depths for this earthquake (see Table 1 and Figure 2). The ISC-EHB report a depth of 17.5 km, although this was fixed *a priori* and so is unreliable, whilst the NEIC reported a depth of 54.0 km, which would place this earthquake in the otherwise-aseismic mid-crust, expected to be the hottest part of the Tibetan crust, posing similar problems to the gCMT depth.

Analysis of teleseismic arrivals at the Warramunga, GERESS and ILAR arrays, along with selected broadband waveforms (Figure 3) shows no arrivals after the direct $P$-wave arrival at times consistent with depth phases from an earthquake at 96.3 km. For all of these three arrays, based on the radiation pattern predicted by the gCMT moment tensor (see Figure 3), we would expect significant energy to be present in the $pP$ depth phase, with a smaller $sP$. The absence of a visible depth phase where the direct arrival is clearly visible is unexpected, if the depth were correct. In the beams for all three arrays, there is some suggestion of a discrete arrival $\sim$3 seconds after the onset of the direct arrival, and, although on none of the beams is this distinct enough to be robustly identified as a depth phase. Similarly, arrivals approximately 3 seconds after the direct arrival are visible on the filtered broadband waveforms shown, most notably from stations ARU, MHV and YAK. When combined with lack of any clear coherent signal in the beam more than 10 seconds after the $P$-wave onset, this suggests a much shallower source depth, probably $\leq$ 10 km. On Figure 3d–g, dashed green traces shown broadband synthetics calculated with shallow (4,6 km) source depths.

Regional waveform inversion (Figure 4) paints a similar picture. For this earthquake, we draw on data from an IRIS/PASSCAL deployment across central Tibet (FDSN code XF), along with sparse other stations (e.g., IC.LSA), offering 37 three-component stations with good-quality waveforms within 1000 km of the earthquake (Figure S1). In Figure 4, we show waveform fits at two selected stations, XF.H1090 and XF.H1508, located $\sim$ 250 km to the west and $\sim$ 450 km to the northwest respectively. Crucially, both vertical and radial components at both stations show strong arrivals associated with both the $P$-wave and the combined $S$/surface-wave arrivals. At shallow depths, a normal-faulting mechanism produces synthetics able to fit the timing, separation, and amplitude of both sets of arrivals. However, at greater depths, and particularly at 50 km and deeper, synthetic waveforms lack the amplitude to fit the later half of the waveform, due to the decrease the amplitude of the modelled surface waves, and also lose the shape to fit the first half. This leads to a best-fit solution at fixed depths of 70 – 90 km using a higher magnitude to increase the amplitude of the $P$-wave group, and fitting part of the complex internal waveform with what should be the first arriving phases – a misidentification that leads to a reduction in the overall misfit, and hence a local misfit minimum (particularly evident on the vertical and radial waveforms at 90 km depth on Figure 4).

Even at shallow depths, the notable degradation in fit between the best-fit solution (at a depth of 4 km), and the best available mechanism with a fixed depth of 10 km, particularly at XF.H1090, demonstrates that this earthquake must indeed be extremely shallow.

The set of depth-fixed inversions shown in Figure 4 shows that once depth is forced to be deeper than $\sim$ 20 km, the mechanism switches polarity, and instead of the best fit being achieved with a moment tensor dominated by north-south striking normal-faulting, better fits (although still not very good) are achieved with a moment tensor dominated by east-west striking thrust-faulting. The mechanism reported by the gCMT is therefore consistent with the reported centroid depth, but both are very much in error. In Section 6.1, we further assess the reasons for this error.

All of the broadband waveforms shown in Figure 3 show strong downwards first-arrivals in the unfiltered traces. The station positions on the focal sphere on Figure 3 are calculated using the catalogue gCMT depth – calculation using a shallower depth consistent with both our regional waveform inversion and our depth-phase analysis decreases the takeoff angles for teleseismic phases by $\sim$ 30 %, and moves these station positions closer to the centre of the focal sphere. We therefore have a cluster of dilatational first motions grouped around the centre of the focal sphere, clearly inconsistent with the gCMT mechanism (which would predict first motions at all these stations to be compressional) but consistent with a moderately-dipping normal-faulting mechanism, as determined by our regional waveform inversion. In Figure S2, we show that synthetic waveforms calculated with our rCMT mechanism and with source depths of 4 – 6 km are able to fit the 8 cleanest teleseismic waveforms observed, confirming both a normal-faulting mechanisms and a shallow source depth.

Finally, in Figs 9 and S9-11 it can be seen that this earthquake on 2005/08/20 produced clear 20 s period surface waves (the fundamental-mode Rayleigh wave), as expected for a shallow event. It is instructive to compare its seismograms in those Figures with those of the earthquake of 2005/03/26, with a genuine depth of ∼80 km, which, again as expected, produced almost no surface waves at that period (discussed further in Section 4.3).

Overall, our reanalysis of this event radically changes its tectonic implications. Had the reported gCMT mechanism and depth been accurate, placing this earthquake at or below the Moho, and indicating north-south shortening, it would have implied a penetration of the cold (<600 °C) Indian shield beneath Tibet to a position at least 200 km further north than that indicated by the deep seismicity to the south. This would in turn have indicated that thermal calculations, suggesting that India should have heated up beyond 600 °C and become aseismic by that point (Bollinger et al, 2006; Priestley et al, 2008; Craig et al, 2012, 2020; McKenzie et al, 2019a), were in turn wrong. Instead, our results show that this earthquake is entirely consistent with widespread observations of shallow normal faulting across the southern plateau, accommodating arc-parallel extension (Tapponnier et al, 1981; Copley et al, 2010; Elliott et al, 2010).

## 4.2 The 2003/2/11 earthquake

The 2003/2/11 event was reported by the gCMT catalogue as a normal-faulting event with a centroid depth of 46.1 km, which would place it in the mid-crust of the plateau. Both the NEIC and ISC-EHB catalogues reported fixed depths, at 33 and 15 km respectively, which are unreliable. As discussed previously, well-determined seismicity in the central plateau rarely extends below 12–15 km, consistent with the internal heating of the thick crust through radiogenic heat production (McKenzie and Priestley, 2008), leading to high crustal temperatures and aseismic behaviour at comparatively shallow depths. A depth of 46 km would therefore be extraordinary, and warrants re-examination.

Data coverage at regional distances over the Tibetan plateau in 2003 was sparse.

Regional data come from a permanent station at Lhasa and regional deployments in Bhutan, China and Nepal, all distributed through IRIS/PASSCAL (FDSN codes XA, XD, and XF). There was only one station (IC.LSA) within 250 km of this earthquake, and of the 12 stations at regional distances (up to 1000 km), almost all lie to the northwest or southeast, leading to poor azimuthal coverage (see Figure S3). Nonetheless, we use what data are available to undertake regional waveform inversion. Although the limited data available leads to less well-defined constraints on the moment tensor and depth than for the other earthquakes studied here (see Figures 2a and 5), we are able to determine that, whilst the gCMT moment tensor is closely matched by our regional moment tensors, the gCMT depth is substantially deeper than our regional waveform inversion can allow. Our best-fit solution has a $\chi$ value relative to the gCMT moment tensor of 0.91, demonstrating a high degree of similarity between the two moment tensors, although we note that for our regional moment tensor we recover a lower percentage double couple than the gCMT. Indeed, our regional inversion only has a $\gamma$ of 0.52 – a value that, for such a small earthquake, is likely to be a resolution issue, not one relating to true source complexity. To test the impact of the high non-double couple component in our best fit moment tensor, we also run an inversion with the mechanism fixed to be a pure double couple (see Figure 5, Table 1). Whilst this leads to a marginally shallower mechanism, the overall conclusions are unchanged, with this earthquake representing very shallow ($\sim$ 5 km) normal-faulting indicative of east-west extension.

As with the previous event, at depths of 70 – 90 km, a local misfit minimum is achieved in our inversion by increasing the event magnitude, and fitting part of the internal waveform using the higher-amplitude bodywaves that result, to compensate for the disappearance of the surface waves from the $S$-wave packet. Again, this also allows for a rotation in the best-fit mechanism, to allow the most appropriate amplitudes for fitting this subection of the waveform.

To supplement the results of our regional inversion, we draw on a limited amount of teleseismic data. None of the small-aperture arrays show clear evidence for discrete and detectable depth phases. Whilst an absence of evidence is not evidence of absence, this in itself suggests a shallow source where depth and direct phases interact. However, several broadband instruments recorded waveforms where there is evidence for the arrival of a depth phase at $\sim$ 4 seconds after the direct arrival. In Figure S4, we show synthetic waveforms for four depths – that from our rCMT inversion, from the ISC-EHB, from the NEIC, and from the gCMT – at four selected stations at teleseismic distances. These demonstrate that only a shallow depth ($\leq$ 7 km), consistent with out rCMT results, is capable of matching the short delay time between the direct arrival and the subsequent depth phases.

In Figure 5, we illustrate the elements of the waveform that rule out the deeper depth reported by the gCMT for this earthquake, and why a shallower depth is required. Despite the similarity in mechanisms, we recover a best-fit depth of 4.8 km, more consistent with the regional seismicity than the gCMT centroid of 46.1 km. As Figure 5 shows, with increased depth, the fit to all three components at the selected stations shown degrades rapidly between 10 and 30 km, with the deeper sources notably unable to fit the observed amplitude of the $S$-wave group and $Lg$, particularly on the vertical and radial components. The sparsity of data leads to a substantially wider distribution of acceptable depths in the PDF shown in Figure 2a than for other events, but the gCMT depth remains far deeper than any acceptable regional waveform solution.

Matching with the results of our regional and teleseismic results, the far-regional surface waves shown in Figure 9 (and Supplementary Figures S9–S11) show substantial surface-wave amplitudes, indicative of a shallow source depth, and inconsistent with a lower-crustal source.

As with the 2005/8/20 event, our reanalysis of the 2003/2/11 event changes its geodynamic implications. Instead of occurring in the hot Tibetan mid-crust – a place where we would not expect earthquakes at all due to the elevated temperature – this earthquake instead has a shallow depth, entirely consistent with the depth of other shallow earthquakes across Tibet.

## 4.3 The 2005/3/26 earthquake

On the $26^{th}$ March 2005, this $M_w \sim 4.7$ earthquake was reported at a depth close to the Moho beneath the central Himalayas. The routine gCMT inversion determined a strike-slip faulting mechanism, with a centroid depth of 70 km – consistent with other travel-time based catalogues, which determined depths of 70.7 km (NEIC), 77.3 km (ISC-EHB) (see Figure 2b).

Figure 6 shows our regional waveform analysis for this earthquake. As with the 2005/8/20 event, our regional inversion is reliant on data from the IRIS/PASSCAL XF network, along with a small number of independent stations (e.g., IC.LSA) – these offer 27 three-component stations with good-quality waveforms within 1000 km (see Figure S5). Our regional centroid inversion yielded results consistent with the gCMT, with a marginally-deeper best-fit depth of 78.3 km, and a very similar strike-slip mechanism, with a similarity index between the two moment tensors of $\chi = 0.96$ – easily within the tolerance of the different data used in each inversion, and the level of noise present for events of this magnitude. The waveform analysis shown in Figure 6 clearly shows that at shallow depths, whilst some of the details of all three components at IC.LSA can still be fit by a shallow, rotated moment tensor, only solutions with a significantly greater depth are able to fit the waveform across multiple phases through the full length of the inversion window. Shallower than 70 km depth, fits degrade rapidly for all three components at both stations shown. For a deeper solution at 90 km depth, we start to see the misalignment of phases, most notable in the radial component at IC.LSA.

We note that our regional inversion fits a best-fit epicentre $\sim 50$ km to the south of the gCMT catalogue location (and ~60 km to the south of arrival-time based catalogues. As shown in Figure S5, the distribution of stations at regional distance for this earthquake covers a relatively small azimuthal range, and is concentrated a significant distance to the north. In our inversion, the source latitude trades off approximately linearly against the origin time - in addition to being 50 km further south our best fit solution has an origin time $\sim 5$ seconds earlier than the gCMT. Fixing the location to that of the gCMT results in only small changes in the mechanism and depth we retrieve, and has no impact on the tectonic implications of this earthquake.

Inspection of broadband instruments at teleseismic distances shows little evidence of discernible depth phases, with only the arrays at GERESS (Germany) and Warramunga (Australia) showing evidence for depth phases consistent with the depths from our regional inversions (see Figure S6, and Craig et al (2012)).

This deeper event does offer a chance to emphasise the difference in surface waves generated between events with a genuinely deep source, and those with sources in the upper crust. In contrast to the two shallow events discussed previously, the 2005/3/26 shows very weak fundamental-mode Rayleigh wave arrivals at far-regional distances (see Figures 9), consistent with its genuinely deep source depth. The surface waves for 2005/8/20 are significantly lower in amplitude than those for the other three events (after normalisation to a common observing distance and magnitude), consistent with a substantially deeper earthquake source for the 2005/8/20 event. This observation is true for all four stations we show results from (Figures 9, S9–S11), which cover a range of azimuths, confirming that this is not simply due to proximity to a nodal plane for the 2005/3/26 event, and suggesting that its source is indeed significantly deeper than for the other three events considered.

Figure 2b shows that the differences in source depths estimated by different methods is small (<10 km). The gCMT solution and NEIC depth lie only just outside of the probability density function from our regional moment tensor inversion. This minor discrepancy between our result and the gCMT is likely to arise from the slightly different data used in each inversion, and the different velocity structures (global and regional) assumed, and is not significant.

In this case the original gCMT depth and focal mechanism are clearly approximately correct, although as we shall see, they were poorly constrained (see Section 6.1). We include its analysis here to point out that there was no *a priori* reason to discount the similar gCMT depth of the 2005/08/20 earthquake (Section 4.1), apparently at 96 km but in fact at shallower than 10 km.

This reinforces our conclusion that an apparent anomaly must be checked before it is believed.

## 4.4 The 2008/6/19 earthquake

The $19^{th}$ June 2008 earthquake is reported in the gCMT catalogue with a predominantly strike-slip faulting moment tensor, including a slight component of E-W extension, and a shallow source depth (see Figure 1). The centroid depth reported is 18.3 km, which would place it at the deeper end of the well-determined shallow seismicity on the Tibetan Plateau, which generally stops at 12 – 15 km. The orientation of the best double-couple nodal planes derived from this moment tensor, striking NNW-SSE and ENE-WSW, are slightly oblique to the region geological features, dominated by normal faulting with a strike NNE-SSW, and strike slip faulting with planes striking NNE-SSW and WNW-ESE, but otherwise, this earthquake is fairly unremarkable amongst the general background seismicity.

Data at regional distances for this event mainly comes from the INDEPTH IV experiment (FDSN codes XO and X4) and an experiment run by the University of Rhode Island in NE Tibet (FDSN code ZV). Along with available continuously operating instruments, these total 56 three-component stations within 1000 km (see Figure S7). In Figure 7, we show waveforms from two to the northeast (XO.AF033) and southeast (X4.F15), for the best-fit solution, and for the best-available moment tensor at a range of fixed depths. The best fit solution, and that with a depth fixed at 10 km, both do a good job of fitting the available waveforms, although the vertical and radial components at X4.F15 show a notable degradation of the fit to all sections of waveform even at 10 km, as expected given the narrow PDF for depth shown in Figure 2d. At depths greater than 10 km, the fit to the details, and particularly amplitude, of the waveforms shown becomes progressively worse.

In Figure 8, we show processed waveform data from three small-aperture seismic arrays at teleseismic distances from this event. Vertical lines show the predicted depth-phase arrivals (for $pP$ and $sP$) based on the gCMT depth of 18.3 km, aligned relative to the $P$-wave onset. All four of these arrays show clear, coherent $P$ arrivals at the correct azimuth and slowness. All four arrays also show the arrival of an additional phase, which we interpret to be a depth phase, $\sim$3-4 seconds after the $P$ onset, several seconds earlier than any of the predicted depth phase arrivals for an 18.3 km source depth. This early-arriving depth phase is consistent with a depth shallower than that reported by the gCMT, and matches the 4–6 km suggested by our regional moment tensor inversion. In Figure S8, we show synthetic waveforms for three broadband stations, calculated with a source depth of 6 km, where this depth phase is matched by the $pP$ arrival.

We note that the gCMT moment tensor for this event has a low percentage double couple, suggestive of a poorly-resolved moment tensor. The regional best fit moment tensor determined here has a much higher percentage double couple, and matches very closely to the mechanism from our pure-double couple inversion (see Figure 7 and Table 1). The moment tensor recovered from our regional waveform inversion is somewhat similar to that from the gCMT catalogue, with a $\chi$ value of 0.78, but has rotated slightly such that the dominant component of deformation is ESE-WNW extension. This matches much better with the orientation of local normal faulting, and potentially changes the interpretation of this earthquake from being a strike-slip faulting earthquake oblique to the local geological structures, and slightly mis-aligned with the focal mechanisms of other nearby seismicity, to a predominantly normal-faulting event, more broadly consistent with the regional deformation.

In conclusion, our preferred depth of about 6 km is clearly shallower than that of the gCMT at 18 km. The shallower depth is no surprise, given the very small elastic thickness estimate of about 4 km (McKenzie et al, 2019b), but the difference of $\sim$12 km between our two estimates is also no surprise, as the gCMT would not claim to resolve the depths of shallow earthquakes to better than at anyway (see also Engdahl et al, 2006). We include this analysis only to show that, if a more precise depth is required for shallow earthquakes, it is necessary to analyze the waveforms at higher frequencies than is typically used by the gCMT, as we have done here.

# 5 Dependence on velocity structure

Regional waveform inversion, such as that carried out above, can be very sensitive to the details of the crustal velocity structure, which essentially acts as a waveguide over such distances (< 1000 km). The approach we use relies on the assumption that a 1-dimensional velocity structure is a reasonable regional average, and that the velocity structure used is appropriate for all ray paths. Although more modern, higher-resolution lithospheric velocity models exist for the Tibetan plateau (e.g., Chen et al, 2017; Gilligan and Priestley, 2018), CRUST2 represents a reasonable average on the 100's – 1000 km scale of our ray paths. We also note that the majority of the stations used for each event (see Supplementary Figures S1,S3,S5,S7) lie within the plateau itself, minimising problems associated with paths that cross the plateau boundary, and propagate through both the thick, slow crust of the plateau, and the thinner, faster crust of the surrounding regions.

In Figure 10, we show results from set of tests for two of our earthquakes (2005/3/26 and 2005/8/20), in which we arbitrarily vary the depth of the Moho by ± 10 km, and the values of the crustal velocities by ± 5%, recompute our Green's functions and rerun our inversion approach. Figure 10 shows probabilistic moment tensors and depth probability density functions for the five velocity models we test, for both events. As we can see, variations in the velocity structure on this order have little impact on the resultant moment tensor, with only minor variations between either the best-fit solution, or the PDF for each different velocity structure. The principal difference between results from different velocity structures is in the depth PDF's – whilst those for the 2005/8/20 event (erroneously located at 96 km) are consistent with the revised shallow depth of about 5 km (see Table 1), the results for the 2005/3/26 event (genuinely at about 75 – 80 km depth) show significant variability, particular in terms of how well-defined the PDF is. For velocity structures with a thicker, or faster, crust, the PDF broadens significantly, with a secondary minimum starting to emerge at shallow depths. However, in all 4 tests for the 2005/3/26, the best-fit solution and principal depth minimum, occur around the depth of the Moho, consistent with our initial result. Whilst there are inherent variations in the actual depth recovered related to uncertainties in the velocity structure, the geological context and interpretation of neither event changes as a result of our velocity-variation tests.

# 6 Discussion

The four events studied here highlight some potential issues with routinely-determined gCMT solutions, most notably for the over-estimation of source depth, and, in rare cases, for the determination of solutions confined to a local minimum in misfit that are not representative of the true source characteristics of the earthquake. These problems are particularly notable for events at the smaller-magnitude end of the range considered by the gCMT. Such events generally have lower signal-to-noise levels, and also lower energy output in the relatively low-frequency bands considered in gCMT moment tensor inversion.

Some of these issues may be mitigated by the increasing density of seismological instrumentation. In many areas of the world, earthquakes today are recorded by a far greater number of near-field seismometers than in 2003, 2005, or 2008. Even in remote, sparsely-instrumented areas, coverage is occasionally supplemented by short-term seismological field experiments (as was the case for the 2008/6/19 earthquake studied here). Indeed, for an earthquake in central Tibet in mid 2020 or mid 2021, only 5 stations at regional distances currently have provided data to the combined FDSN repositories – a substantial decrease in the level of data available for the event from 2008 studied here.

Our study demonstrates that in certain cases, moment tensors and locations from the gCMT (and other automated location routines) may be subject to substantial non-systematic errors. As seen for the 2005/8/20 earthquake, this can lead to errors in both moment tensor and in depth. In cases where the focal mechanisms of individual events are clearly anomalous against the regional trend, we therefore consider it necessary to re-examine the details of the waveforms, and confirm the appropriateness of the solution, before basing any geophysical interpretation on such events.

In comparing our regional CMT inversion results with those from the gCMT catalogue, we note that in all cases we report a slightly lower magnitude than the gCMT (see Table 1). However, in the cases of the two earthquakes where our depth estimates are most similar this difference is only 0.1 magnitude units (within acceptable uncertainty, given the different elastic structures used in each case), whereas for the two events where we recover a substantially shallower centroid depth than the gCMT (2003/2/11 and 2005/8/20), our magnitude estimates are 0.4 and 0.5 lower than the gCMT. This difference in magnitude may perhaps result from the gCMT approach fitting significant energy from the higher amplitude $S$- and surface wave arrivals with the $P$-wave arrivals, and hence increasing the magnitude to provide sufficient amplitude in the $P$ waves.

Of the four events we consider, only one was accurately characterised by the gCMT, ISC-EHB, or NEIC catalogues (the 2005/3/26 event). The other three had the potential to change our understanding of the structure and dynamics of Tibet, either through their location, their mechanism, or both. However, all were in fact consistent with our current understanding of Tibetan tectonics, and no such reassessment is warranted on the basis of these earthquakes. The 2003/2/11 and 2005/8/20 events are in fact at shallow depths, entirely consistent with the regional seismogenic thickness. The 2005/8/20 event is not indicative of N-S shortening, but of E-W extension, and has an orientation that fits with the alignments of south Tibetan rifting. The 2008/6/19 event has a shallow depth, consistent with the regional seismogenic thickness, and a mechanism orientation consistent with the regional extensional strain.

## 6.1 What went wrong in the gCMT analysis?

For three of the four events investigated in detail in the current study, the source parameters determined here differ substantially from those in the gCMT catalogue. As it is reasonable to believe that the results from our detailed investigation provide better descriptions of these earthquakes, the logical question then becomes whether explanations exist for the low quality of the published gCMT results, or for the inclusion of those results in the gCMT catalogue.

To address this, we first describe the procedure by which earthquakes are added to the gCMT catalogue and then review the details of the four earthquakes in the this context. We also perform a reanalysis of the four events using current gCMT procedures (results shown in Tables S1 and S2).

The goal of the Global CMT Project is the systematic determination of source mechanisms of earthquakes with magnitudes 5.0 and larger occurring globally. More than 300 earthquakes are analyzed each month and, in a typical month, two thirds of the events are judged to have sufficiently well-constrained source parameters to be acceptable for inclusion in the gCMT catalogue. While most of the CMT analysis is semi-automatic, the results for each earthquake are reviewed by the analyst and one of the Principal Investigators before inclusion in the catalogue. To make the review efficient, numerical criteria based on (1) the stability of the inversion results, (2) the number of seismograms that can be fit, and (3) the overall quality of the fits, are applied to make a selection. Each earthquake is viewed in its geographical context, and tectonic plausibility is used as an additional criterion, so that earthquakes with unusual mechanisms are subjected to additional scrutiny and analysis. The operational objective is to include only reliable solutions, and to exclude earthquakes with marginal results. Notwithstanding these efforts, low-quality and erroneous mechanisms exist in the gCMT catalogue. Human error may occasionally lead to the wrong earthquake being included and, more commonly, the event review may lead to an incorrect assessment of the quality of the result.

### The 2005/8/20 earthquake

For this event, both the gCMT mechanism and the centroid depth are grossly different from the results presented in this study. The inversion results for this earthquake did not meet one of the current (since around 2006) quality criteria when it was included in the CMT catalogue. Specifically, only 85 well-fit seismograms were included, when the required minimum is now 100. In addition, in meeting the 'tectonic plausibility' criterion, the highly unusual reverse mechanism should have been noticed and led to a careful review. The erroneous inversion results can plausibly be traced back to a starting depth of 54.0 km in the gCMT analysis (based on the initially-reported PDE depth from the NEIC). In the initial gCMT inversion steps, the centroid moved to a greater rather than a smaller depth, to find a local misfit minimum at 96.3 km. At this depth, a subset of the intermediate-period Love and Rayleigh waves can be fit adequately with a reverse mechanism rotated 90 degrees with respect to the correct normal-faulting mechanism. It is worth noting that for a larger earthquake the broad frequency content of signals above the noise level typically is sufficient to move the earthquake to the correct depth, even when the starting hypocenter is wrong. For events smaller than M5.0, such as this event, this does not always happen.

When this earthquake is reanalyzed using the current gCMT algorithm and using the ISC starting depth of 29.1 km, the inversion converges automatically to a normal-faulting solution with a geometry similar to that determined in the current study, and a shallower depth of 20.3 km, with 152 well-fit seismograms.

### The 2003/2/11 earthquake

The anomalous centroid depth of 46.1 km reported in the gCMT catalogue is a consequence of the way the excitation of seismic waves is calculated in the gCMT algorithm, and the types of data that were included in the inversion. Specifically, wave excitation is calculated in a spherically symmetric Earth model with an average crustal thickness. The difference between the true velocity structure and the model velocity structure leads to a bias in the centroid depths for earthquakes occurring in regions with exceptionally thick crust, such as Tibet, with the estimated depth greater than the true depth. This bias is particularly strong when only long-period body waves are included in the inversion, as was the case for moderate earthquakes before 2004. For earthquakes from 2004 onwards, intermediate-period surface waves are included in the CMT inversions. This has improved the estimation of depth in all areas, including in Tibet. For the 2003/2/11 earthquake, only body waves were included. It is worth noting that even though the gCMT depth is much too deep, the focal mechanism is similar to that obtained in the detailed investigation.

When this earthquake is reanalyzed using the current gCMT algorithm, which includes the intermediate-period suface-wave data, the focal mechanism is not much changed, but the centroid depth is significantly shallower at 17.9 km.

### The 2005/3/26 earthquake

This earthquake is smaller than M5.0 and the inversion results did not meet the current criterion for the number of well-fit seismograms with only 85 good seismograms. The estimated depth (69.6 km) is close to the starting depth (70.7 km), which may reflect limited depth sensitivity of the waveforms that were included. When this earthquake is re-analyzed using our current algorithm and a starting depth of 54.7 km from the ISC, the CMT converges to a depth of 49.1 km. However, the number of well-fit waveforms remains below 100 and it therefore would not satisfy the quality criterion for inclusion in the modern gCMT catalogue.

It worth highlighting here that the original gCMT solution for this event, although approximately correct in both depth and mechanism, (a) differs from the solution derived using the modern gCMT approach and (b) that this solution would have been insufficiently well-constrained to have made it into the final catalogue. Hence, even for events that fit the background trend, when such events are small and/or poorly-constrained, we still urge caution, and where possible, independent verification.

### The 2008/6/19 earthquake

This earthquake met all quality criteria when it was included in the catalog. A reanalysis leads to a very similar mechanism and depth to that included in the gCMT catalog, with a centroid depth of 18.8 km, and matches well with the results presented earlier in this study.

### Summary of gCMT reanalysis

The reverse-faulting mechanism reported for the 2005/8/20 earthquake in the gCMT catalog is wrong and, using current review criteria, the earthquake would either not have been included in the catalog, or an analysis would have been attempted at shallow depth, most likely leading to an acceptable result. The large depth estimated for the 2003/2/11 earthquake is consistent with a pattern of bias seen for earthquakes in regions with thick crust. Inclusion of intermediate-period surface waves improves the depth estimate. Other earthquakes in the CMT catalog for the period prior to 2004 may exhibit a similar depth bias. The 2005/3/26 is a marginal earthquake for CMT analysis, and would not have been included in the catalog using current selection criteria. The 2008/6/19 earthquake is a small earthquake for which the published CMT solution provides an adequate source characterization.

# 7 Conclusions

The routine determination of centroid moment tensors for moderate- and large-magnitude earthquakes over the last six decades has been one of the great resources in solid-Earth geophysics, and has revolutionised our understanding the distribution, style, and mechanism of earthquakes, and how these reflect regional tectonics. It is now much easier to spot earthquakes that are apparently anomalous and stand out from the general pattern of seismicity, and these are always worth noting, as they have revealed important geodynamic and tectonic insights in the past. But our study highlights the need to carefully interrogate – manually if necessary – individual anomalous and significant earthquakes, especially smaller magnitude ones, before using these to underpin new geological or geophysical interpretations.

# Acknowledgements

TJC was supported in this work by the Royal Society under URF\R1\180088. TJC was also supported through COMET, the UK Natural Environment Research Council's Centre for the Observation and Modelling of Earthquakes, Volcanoes, and Tectonics. Maps in this paper are created using GMT software (Wessel and Smith, 1998). Seismological processing and plotting used the routines of Beyreuther et al (2010) and Heimann et al

(2018).

We thank the editor (Margarita Segou), and three reviewers (Steven Roecker, Andreas Steinberg, and one anonymous reviewer) for their comments on the manuscript.

# Data Availability

All data used in this study are open access and publicly available. We draw on seismological data from a number of networks, principally AU, CN (`doi:10.7914/SN/CN`), GE (`doi:10.14470/TR560404`), IC (`doi:10.7914/SN/IC`), IM, XA (`doi:10.7914/SN/XA_2002`), XD (`doi:10.7914/SN/XD_2002`), XF (`doi:10.7914/SN/XF_2002`), XO, X4 (`doi:10.7914/SN/X4_2007`), and ZV (`doi:10.7914/SN/ZV_2008`). We are indebted to those involved in the maintenance of these networks.

# References

Bassin C, Laske G, Masters G (2000) The Current Resolution for Surface Wave Tomography in North America. EOS Transactions, AGU 81

Beyreuther M, Barsch R, Krischer L, Megies T, Behr Y, Wassermann J (2010) ObsPy: A Python Toolbox for Seismology. Seismological Research Letters 81:530–533, DOI 10.1785/gssrl.81.3.530

Bollinger L, Henry P, Avouac JP (2006) Mountain building in the Nepal Himlaya: Thermal and kinematic model. Earth and Planetary Science Letters 244:58–71, DOI 10.1016/j.epsl.2006.01.045

Chapman C (1978) A new method for computing synthetic seismograms. Geophysical Journal of the Royal Astronomical Society 45:481–518

Chapman C, Yen-Li C, Lyness D (1988) The WKBJ seismogram algorithm. In: Doornbos D (ed) Seismological algorithms: Computational methods and computer programs, Academic Press Limited, London, pp I.2,47–74

Chen M, Niu F, Tromp J, Lenardic A, Lee CTA, Cao W, Ribeiro J (2017) Lithospheric foundering and underthrusting imaged beneath Tibet. Nature Communications 8, DOI 10.1038/ncomms15659

Chen WP, Molnar P (1983) Focal depths of intracontinental and intraplate earthquakes and their implications for the thermal and mechanical properties of the lithosphere. Journal of Geophysical Research 88:4183–4214

Copley A, Avouac J, Royer J (2010) India-Asia collision and the Cenozoic slowdown of the Indian plate: Implications for the forces driving plate motions. Journal of Geophysical Research 115, DOI 10.1029/2009JB006634

Copley A, Avouac JP, Wernicke BP (2011) Evidence for mechanical coupling and strong Indian lower crust beneath southern Tibet. Nature 472:79–81, DOI 10.1038/nature09926

Craig T, Methley P, Sandiford D (2022) Imbalanced moment release within subducting places during initial bending and unbending. Journal of Geophysical Research 127, DOI 10.1029/2021JB023658

Craig TJ, Jackson J (2021) Variations in the Seismogenic Thickness of East Africa. Journal of Geophysical Research 126, DOI 10.1029/2020JB020754

Craig TJ, Copley A, Jackson J (2012) Thermal and tectonic consequences of India underthrusting Tibet. Earth and Planetary Science Letters 353-354:231–239, DOI 10.1016/j.epsl.2012.07.010

Craig TJ, Kelemen P, Hacker B, Copley A (2020) Reconciling geophysical and petrological estimates for the thermal structure of Southern Tibet. Geochemistry, Geophysics, Geosystems 21, DOI 10.1029/2019GC008837

Dziewonski A, Woodhouse J (1983) An experiment in the systemiatic study of global seismicity: centroid-moment tensor solutions for 201 moderate and large earthquakes of 1981. Journal of Geophysical Research 88:3247–3271

Dziewonski A, Chou TA, Woodhouse J (1981) Determination of earthquake source parameters from waveform data for studies of global and regional seismicity. Journal of Geophysical Research 86:2825–2852

Ekstrom G, Morelli A, Boschi R, Dziewonski A (1998) Moment tensor analysis of the Central Italy Earthquake Sequence of September-October 1997. Geophysical Research Letters 25, DOI 10.1029/98GL01241

Ekström G, Nettles M, Dziewonski A (2012) The global CMT project 2004-2010: Centroid-moment tensors for 13,017 earthquakes. Physics of the Earth and Planetary Interiors 200-201:1–9, DOI 10/1016/j.pepi.2012.04.002

Elliott JR, Walters RJ, England PC, Jackson JA, Li Z, Parsons B (2010) Extension on the Tibetan plateau: recent normal faulting measured by InSAR and body wave seismology. Geophysical Journal International 183:503–535, DOI 10.1111/j.1365-246X.2010.04754.x

Engdahl ER, Jackson JA, Myers SC, Bergman EA, Priestley K (2006) Relocation and assessment of seismicity in the Iran region. Geophysical Journal International 167:761–778, DOI 10.1111/j.l365-246X.2006.03127

Gilligan A, Priestley K (2018) Lateral variations in the crustal structure of the Indo-Eurasian collision zone. Geophysical Journal International 214:975–989, DOI 10.1093/gji/ggy172

Heimann S, Isken M, Kühn D, Sudhaus H, Steinberg A, Vasyura-Bathke H, Daout S, Cesca S, Dahm T (2018) Grond - A probabilistic earthquake source inversion framework. DOI 10.5880/GFZ.2.1.2018.003, URL `http://pyrocko.org/grond/docs/current/`

Isacks B, Oliver J, Sykes L (1968) Seismology and the new global tectonics. Journal of Geophysical Research 73:5855–5899

J Jackson KP D McKenzie (2021) Relations between earthquake distributions, geological history, tectonics and rheology on the continents. Philosophical Transactions of the Royal Society A 37, DOI 10.1098/rsta.2019.0412

Jackson J, Priestley K, Allen M, Berberian A (2002) Active tectonics of the South Caspian Basin. Geophysical Journal International 148:214–245

Langin WR, Brown LD, Sandvol EA (2003) Seismicity of Central Tibet from Project INDEPTH III Seismic Recordings. Bulletin of the Seismoglogical Society of America 93:2146–2159

Liang X, Zhou S, Chen YJ, Jin G, Xiao L, Liu P, Fu Y, Tang Y, Lou X, Ning J (2008) Earthquake distribution in southern Tibet and its tectonic implications. Journal of Geophysical Research 113, DOI 10.1029/2007JB005101

McKenzie D (1972) Active Tectonics of the Mediterranean Region. Geophysical Journal of the Royal Astronomical Society 30:109–185

McKenzie D, Priestley K (2008) The influence of lithospheric thickness variations on continental evolution. Lithos 102:1–11, DOI 10.1016/j.lithos.2007.05.005

McKenzie D, Jackson J, Priestley K (2019a) Continental collisions and the origin of subcrustal continental earthquakes. Canadian Journal of Earth Sciences 56, DOI 10.1139/cjes-2018-0289

McKenzie D, McKenzie J, Fairhead D (2019b) The Mechanical Structure of Tibet. Geophysical Journal International 217, DOI 10.1093/gji/ggz052

Molnar P, Tapponnier P (1975) Cenozoic Tectonics of Asia: Effects of a Continental Collision. Science 189:419–426

Monsalve G, Sheehan A, Schulte-Pelkum V, Rajaure S, Pandey MR, Wu F (2006) Seismicity and one-dimensional velocity structure of the himalayan collisions zone: Earthquakes in the crust and upper mantle. Journal of Geophysical Research 111, DOI 10.1029/2005JB004062

Priestley K, Jackson J, McKenzie D (2008) Lithospheric structure and deep earthquakes beneath India, the Himalaya and southern Tibet. Geophysical Journal International 172:345–362, DOI 10.1111/j.1365-246X.2007.03636.x

Rost S, Thomas C (2002) Array Seismology: Methods and applications. Reviews of Geophysics 40, DOI 10.1029/2000RG0001002002

Ruppert N, Rollins C, Zhang A, Meng L, Holtkamp S, abd JT Freymueller MW (2018) Comple Faulting and Triggered Rupture During the 2018 Mw 7.9 Offshore Kodiak, Alaska, Earthquake. Geophysical Research Letters 45, DOI 10.1029/2018GL078931

Sandiford D, Moresi L, Sandiford M, Farrington R, Yang T (2020) The Fingerprints of Flexure in Slab Seismicity. Tectonics 39, DOI 10.1029/2019TC005894

Schulte-Pelkum V, Monsalve G, Sheehan A, Shearer P, Wu F, Rajaure S (2019) Mantle earthquakes in the Himalayan collision zone. Geology 47:815–819, DOI 10.1130/G46378.1

Shuler A, Nettles M, Ekström G (2013) Global observation of vertical-CLVD earthquakes at active volcanoes. Journal of Geophysical Research 118, DOI 10.1029/2012JB009721

Tapponnier P, Mercier J, Armijo R, Tonglin H, Ji Z (1981) Field evidence for active normal faulting in Tibet. Nature 294:410–414

Wang R (1999) A Simple Orthonormalization Method for Stable and Efficient Computation of Green's Functions. Bulletin of the Seismological Society of America 89:733–741

Wei S, Helmberger D, Avouac JP (2013) Modeling the 2012 Wharton basin earthquake off-Sumatra: Complete lithosphere failure. Journal of Geophysical Research 118, DOI 10.1002/jgrb.50267

Wessel P, Smith W (1998) New, improved version of Generic Mapping Tools released. Eos Trans AGU 79

| Origin time (UTC) | | Method | Lat (°) | Long (°) | Depth (km) | Strike (°) | Dip (°) | Rake (°) | $M_{rr}$ | $M_{tt}$ | $M_{pp}$ | $M_{rt}$ | $M_{rp}$ | $M_{tp}$ | $m_b$ | $\gamma$ | $\chi$ |
|---|---|---|---|---|---|---|---|---|---|---|---|---|---|---|---|---|---|
| | | NEIC | 32.51 | 93.79 | $33.0^f$ | - | - | - | - | - | - | - | - | - | 5.2 | - | |
| | | ISC-EHB | 32.52 | 93.71 | $15.0^f$ | - | - | - | - | - | - | - | - | - | 5.2 | - | |
| 2003/02/11 | 10:36:30.5 | gCMT | 32.55 | 93.67 | 46.1 | 164 | 59 | -108 | -0.603 | -0.024 | 0.628 | -0.212 | 0.275 | 0.010 | 5.2 | 92 | 0.91 |
| | | rCMT | 32.51 | 93.62 | 4.7 | 171 | 62 | -110 | -0.417 | -0.276 | 0.700 | -0.495 | 0.353 | 0.057 | 4.8 | 52 | |
| | | rCMT (DC) | 32.30 | 93.84 | 2.0 | 142 | 78 | -130 | - | - | - | - | - | - | 4.7 | 100 | |
| | | NEIC | 28.26 | 87.93 | 70.7 | - | - | - | - | - | - | - | - | - | 4.9 | - | |
| | | ISC-EHB | 28.22 | 87.84 | 77.3 | - | - | - | - | - | - | - | - | - | 4.8 | - | |
| 2005/03/26 | 20:32:15.7 | gCMT | 28.08 | 87.95 | 69.6 | 109 | 62 | 179 | 0.002 | -0.397 | 0.395 | -0.095 | -0.320 | -0.481 | 4.9 | 97 | 0.96 |
| | | rCMT | 27.63 | 87.91 | 77.1 | 204 | 80 | 021 | -0.059 | -0.411 | 0.471 | 0.074 | -0.334 | -0.431 | 4.8 | 59 | |
| | | rCMT (DC) | 27.63 | 87.87 | 78.3 | 204 | 88 | 017 | - | - | - | - | - | - | 4.7 | 100 | |
| | | NEIC | 31.22 | 88.17 | 54.0 | - | - | - | - | - | - | - | - | - | 5.1 | - | |
| | | ISC-EHB | 31.27 | 88.12 | $17.5^f$ | - | - | - | - | - | - | - | - | - | 5.0 | - | |
| 2005/08/20 | 12:50:48.7 | gCMT | 31.08 | 88.09 | 96.3 | 089 | 44 | 074 | 0.658 | -0.704 | 0.046 | -0.034 | 0.129 | 0.130 | 5.1 | 90 | 0.10 |
| | | rCMT | 30.99 | 88.21 | 4.0 | 169 | 48 | -138 | -0.475 | -0.124 | 0.599 | -0.361 | -0.016 | 0.264 | 4.6 | 97 | |
| | | rCMT (DC) | 30.99 | 88.13 | 3.5 | 171 | 48 | -136 | - | - | - | - | - | - | 4.6 | 100 | |
| | | NEIC | 33.31 | 92.10 | 36.5 | - | - | - | - | - | - | - | - | - | 4.7 | - | |
| | | ISC-EHB | 33.23 | 92.16 | $18.3^f$ | - | - | - | - | - | - | - | - | - | 4.7 | - | |
| 2008/06/19 | 22:36:59.2 | gCMT | 33.13 | 92.19 | 18.3 | 065 | 67 | -016 | -0.284 | -0.312 | 0.595 | -0.091 | 0.145 | 0.452 | 4.7 | 51 | 0.77 |
| | | rCMT | 33.17 | 91.88 | 3.8 | 059 | 73 | -049 | -0.298 | -0.177 | 0.474 | -0.469 | -0.085 | 0.318 | 4.8 | 90 | |
| | | rCMT (DC) | 33.18 | 91.92 | 4.7 | 057 | 72 | -050 | - | - | - | - | - | - | 4.8 | 100 | |

Table 1: Earthquake source parameters from the NEIC, ISC-EHB, and gCMT catalogues and from our regional waveform inversions, both as a deviatoric moment tensor, and constrained to be a pure double couple. Depths reported from the gCMT catalogue here are their centroid depths. Depths from the the ISC-EHB and NEIC marked with $^f$ are fixed during inversion for the other location parameters. Results quoted here for our regional moment-tensor inversion are the best-fit solution, rather than the mean of the PDF. Strike, dip and rake are for the best-double-couple component of the deviatoric moment tensor (see text for definition). Moment tensors reported here are normalised, to allow comparability. $\gamma$ is the percentage double couple, and $\chi$ is the similarity index, as defined in Section 3.

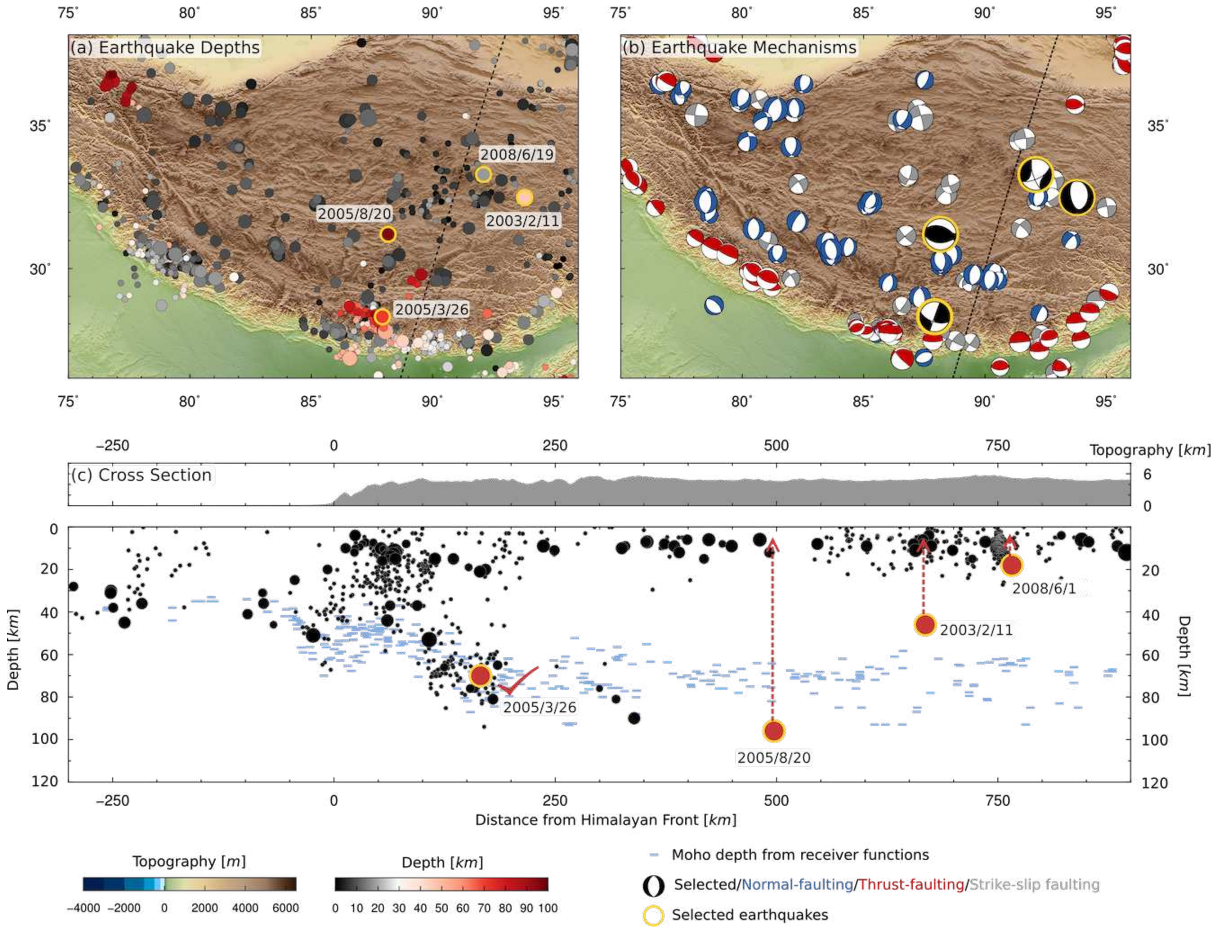


Figure 1: Maps and cross-section to show why the 4 events discussed here are of interest. Data are taken from the compilation of Craig et al (2020), and references therein, and contain only earthquakes with well-constrained source mechanisms and depths from detailed waveform analysis. (a) Earthquake depths across the Himalayas and Tibetan plateau. Yellow outlines highlight the four earthquakes studied here, with their depths taken from the gCMT catalogue, with their dates alongside. Black dashed line shows the section line used in (c). (b) Earthquake focal mechanisms across the Tibetan plateau. Compressional quadrants are shaded based on the type of mechanism, to indicate thrust- (red), normal- (blue, and strike-slip (grey) faulting. Black moment tensors are again those for our four study earthquakes, from the gCMT catalogue. (c) Cross section. Top panel shows the topography over a 10 km wide swath along the line of section shown in (a) and (b). Lower panel shows earthquake depths, as in (a), along with estimates of Moho depth determined by published receiver function studies (see compilation in Craig et al (2020), and references therein) for locations within 500 km of the section line shown in (a) and (b). Red points highlight our four earthquakes of interest, with arrows showing the change in depth from the gCMT catalogue to our redetermined depth.

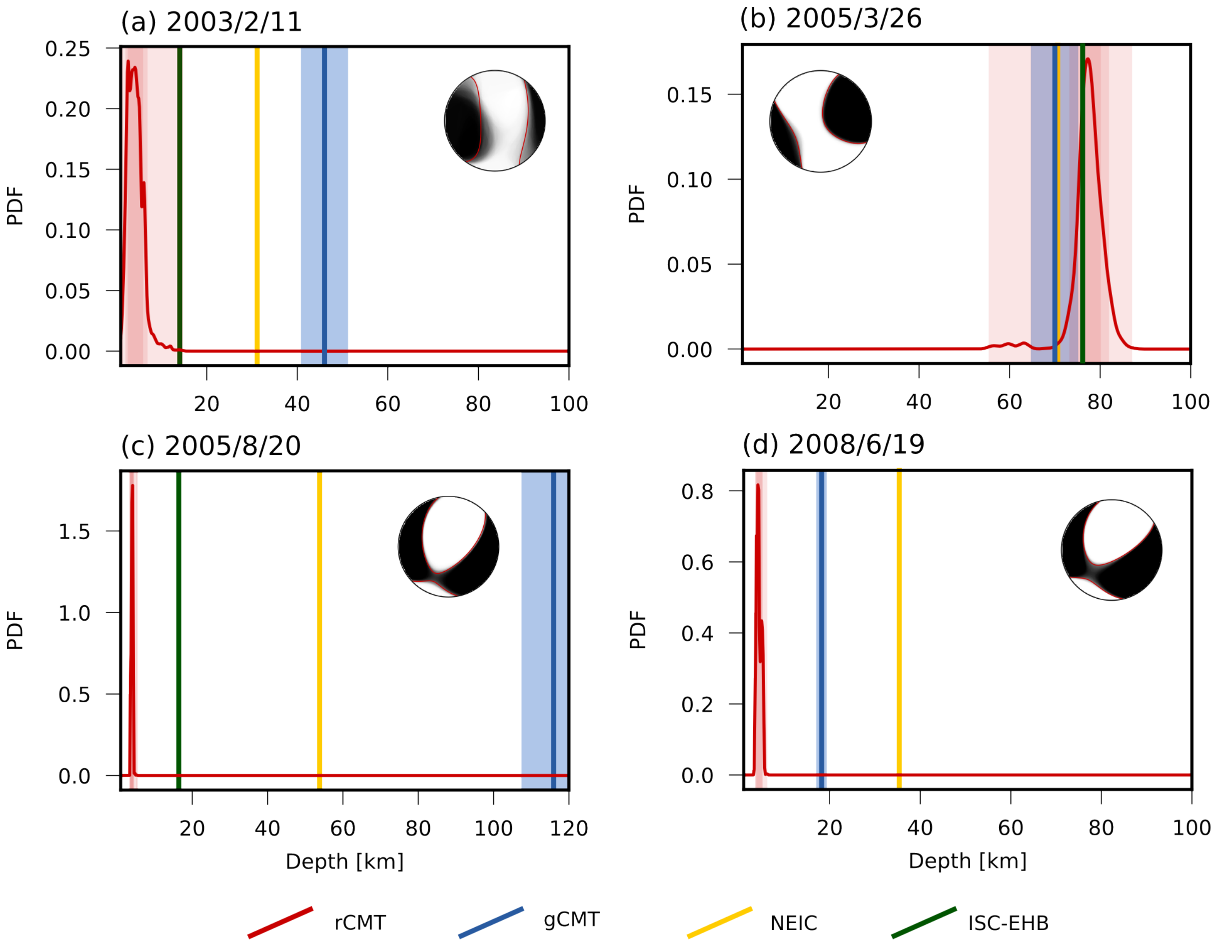


Figure 2: Probability distribution functions for centroid depth for our four study events (solid red lines). Pink shaded areas show the 68% and 90% confident intervals, and minimum/maximum value ranges in order of decreasing intensity. All inversions were run with depth free in the range 1 – 100 km. Blue vertical line indicates the centroid depth from the gCMT catalogue, with the blue shaded area indicating the centroid depth error range. Yellow indicates the depth determined by the NEIC, and green that from the ISC-EHB, as detailed in Table 1. Note that for the 2008/6/19 event the gCMT and ISC-EHB depths are identical (only the gCMT is shown). Inset is the probabilistic moment tensor from our regional inversion, with the best fit solution outlined in red.

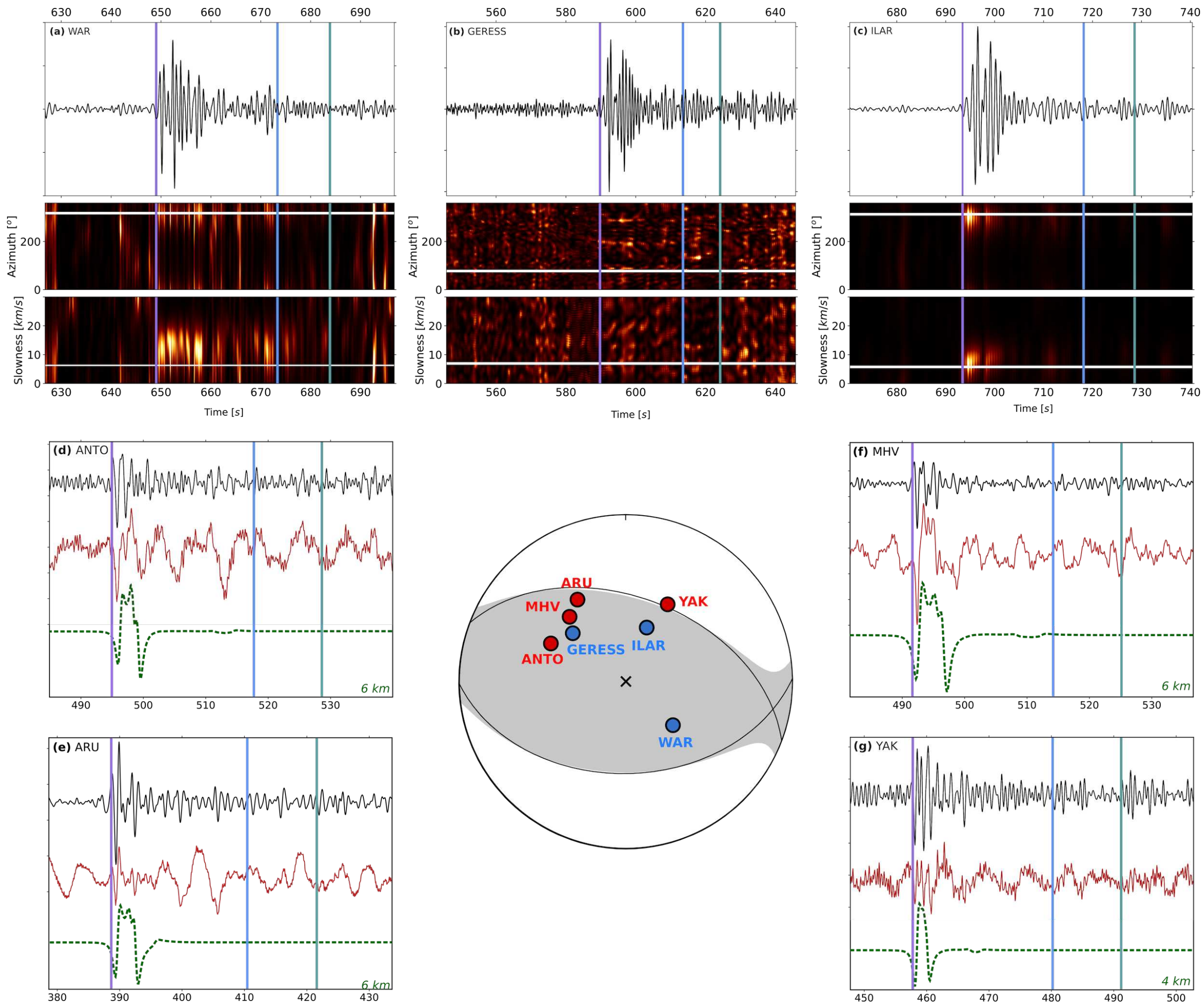


Figure 3: Array processing results for the 2005/8/20 event from arrays at (a) Warramunga Array, Australia; (b) GERESS Array, Germany; (c) ILAR Array, Alaska, USA, and broadband waveforms from (d) ANTO, Turkey; (e) ARU, Russia; (f) MHV, Russia; and (g) YAK, Russia. For each array, upper panel shows the array beam using the predicted backazimuth and slowness, and lower panels show sweeps through backazimuth and slowness space, with the colour scale indicating beam power. White horizontal lines show the predicted backazimuth and slowness. The lower four panels (d–g) show broadband waveforms, black traces are filtered between 0.5 and 2.0 *Hz*, whilst the red trace is unfiltered, dashed green traces are synthetics calculated using our revised mechanism and a source depth of 4 or 6 km (as indicated in the lower left of each panel). On each panel, vertical lines show $P$ (purple), $pP$ (blue), and $sP$ (green) arrivals, using the centroid depth from the gCMT catalogue (96.3 km). Arrival time for $P$ is manually re-picked. The focal mechanism shows the gCMT moment tensor and best double couple, and the station positions on the focal sphere for the arrays (blue) and broadband stations (red) shown.

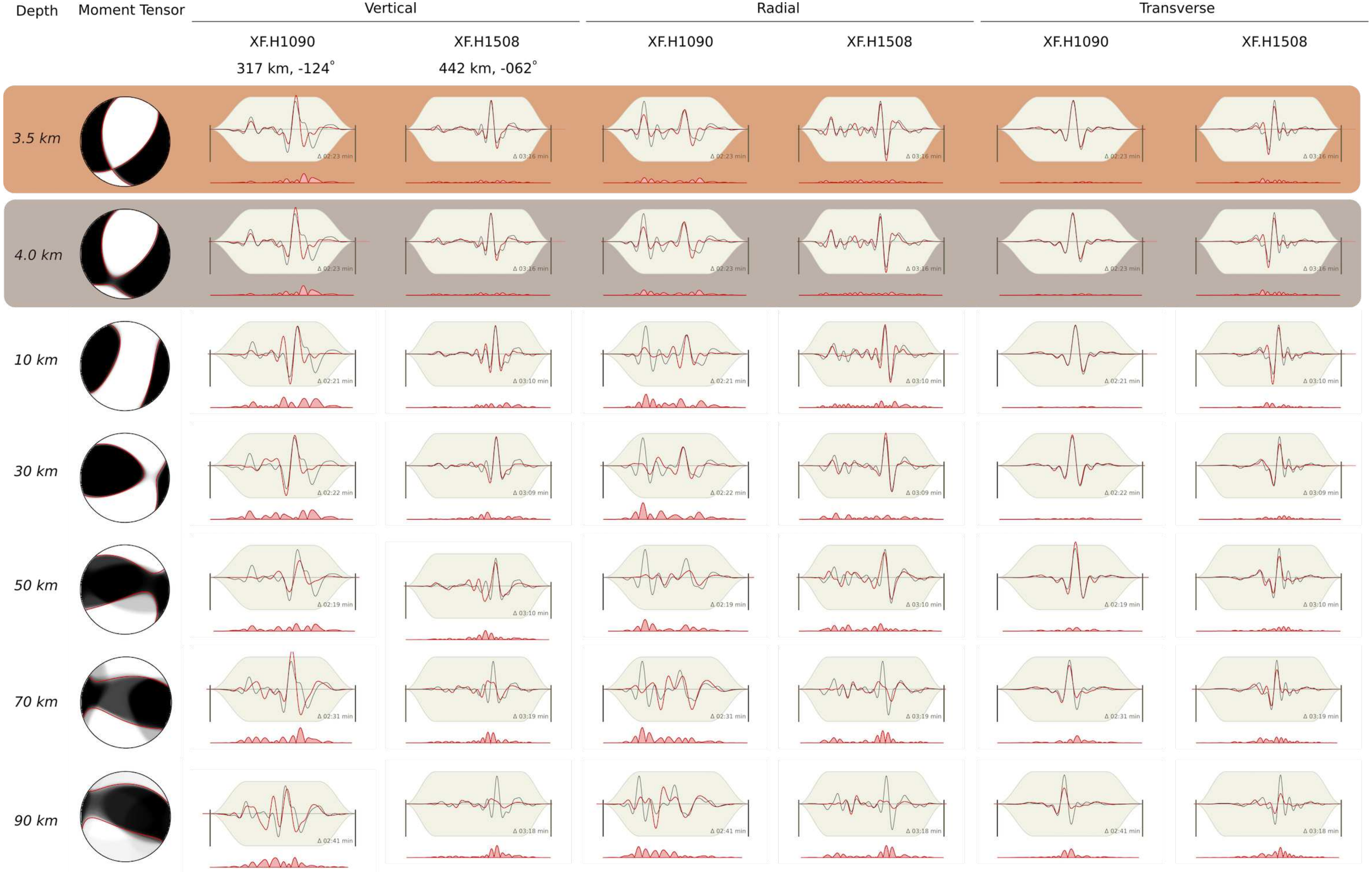


Figure 4: Regional waveform inversion results for the 2005/8/20 earthquake. Grey and tan bars (top two rows) highlight the best-fit solutions from inversions for a deviatoric moment tensor and for a purely double-couple mechanism, respectively. Other rows show inversion results with depth fixed at the value shown in the first column, and all other source parameters free. Second column shows the probabilistic moment tensor, with the best-fit solution highlighted in red. Subsequent columns show observed waveforms (black) and synthetic waveforms (red) for two stations (locations relative to the earthquake are shown at the top of columns 3 and 4), showing the vertical, radial, and transverse components for each station. Beige shaded regions show the section of each trace used in determining the misfit during inversion. Inset text gives the time duration of waveform used in the inversion in each case, which is defined based on the predicted $P$- and $S$-wave arrival times. Red trace along the base of each waveform shows the temporal variation in misfit (amplitude scaling is consistent across all plots).

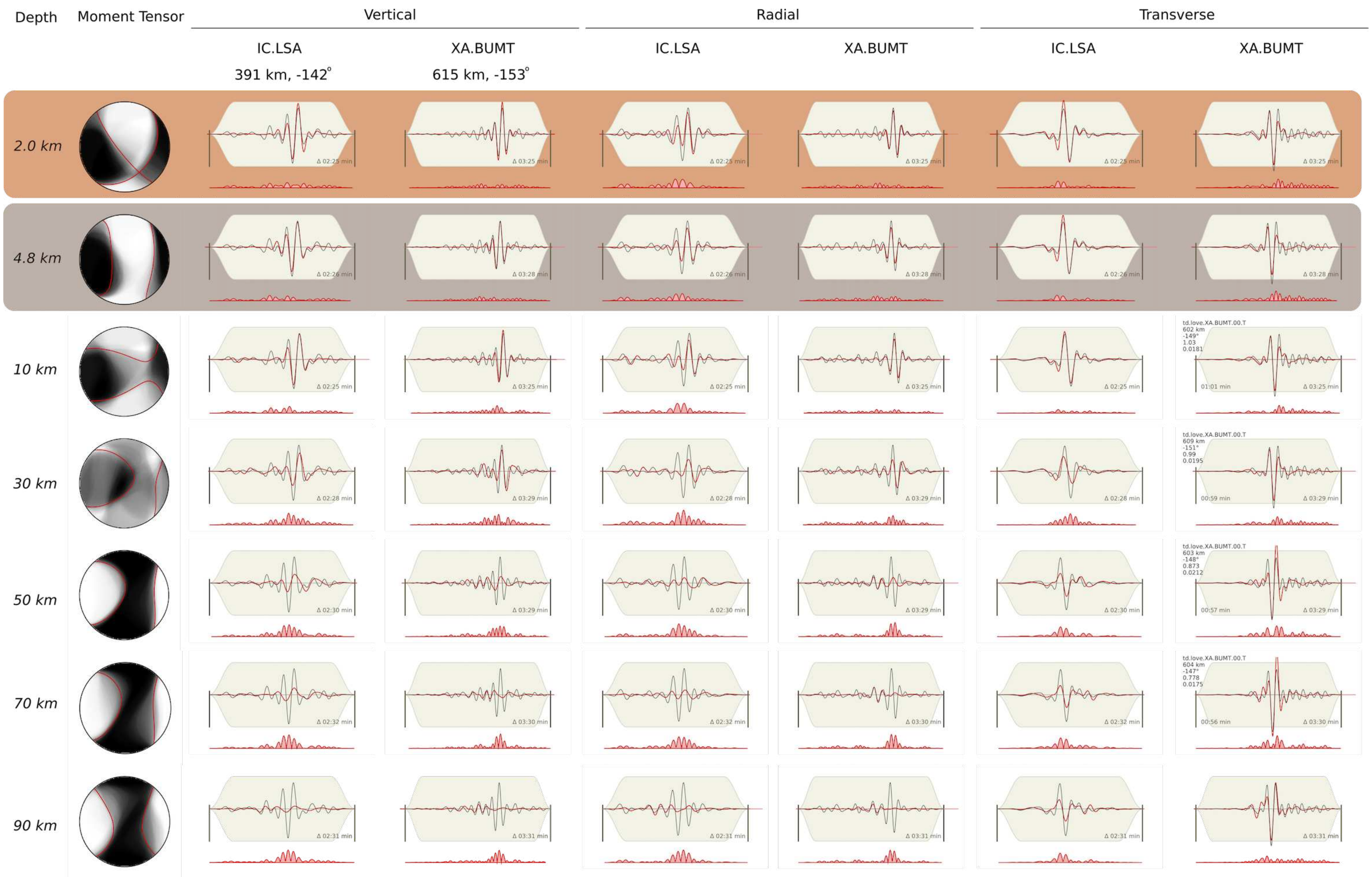


Figure 5: Regional waveform inversion results for the 2003/2/11 earthquake. Caption is as described for Figure 4. Note that the moment tensor shown for the best-double couple solution is probabilistic representation of the PDF of all acceptable double-couple moment tensors.

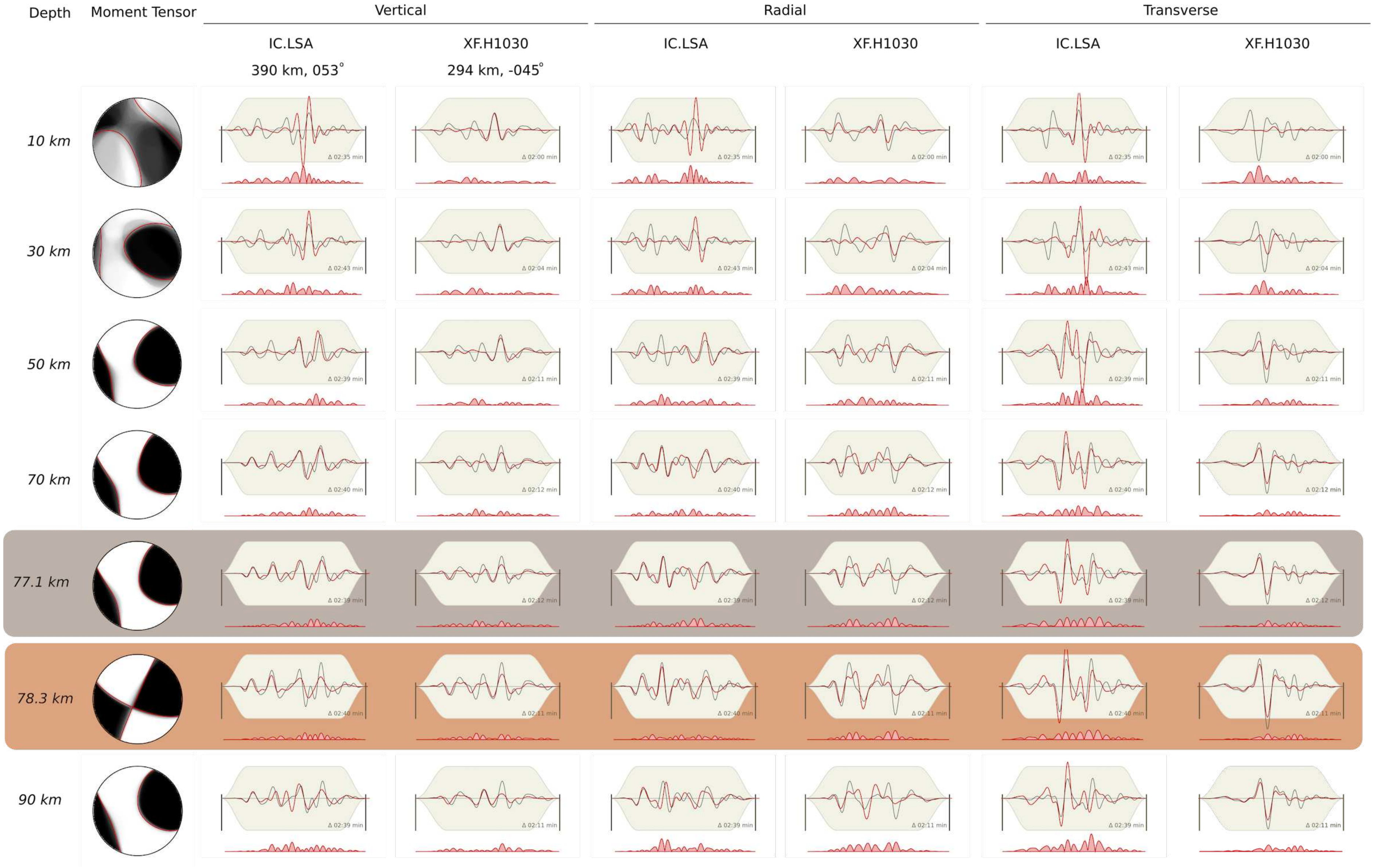


Figure 6: Regional waveform inversion results for the 2005/3/26 earthquake. Caption is as described for Figure 4.

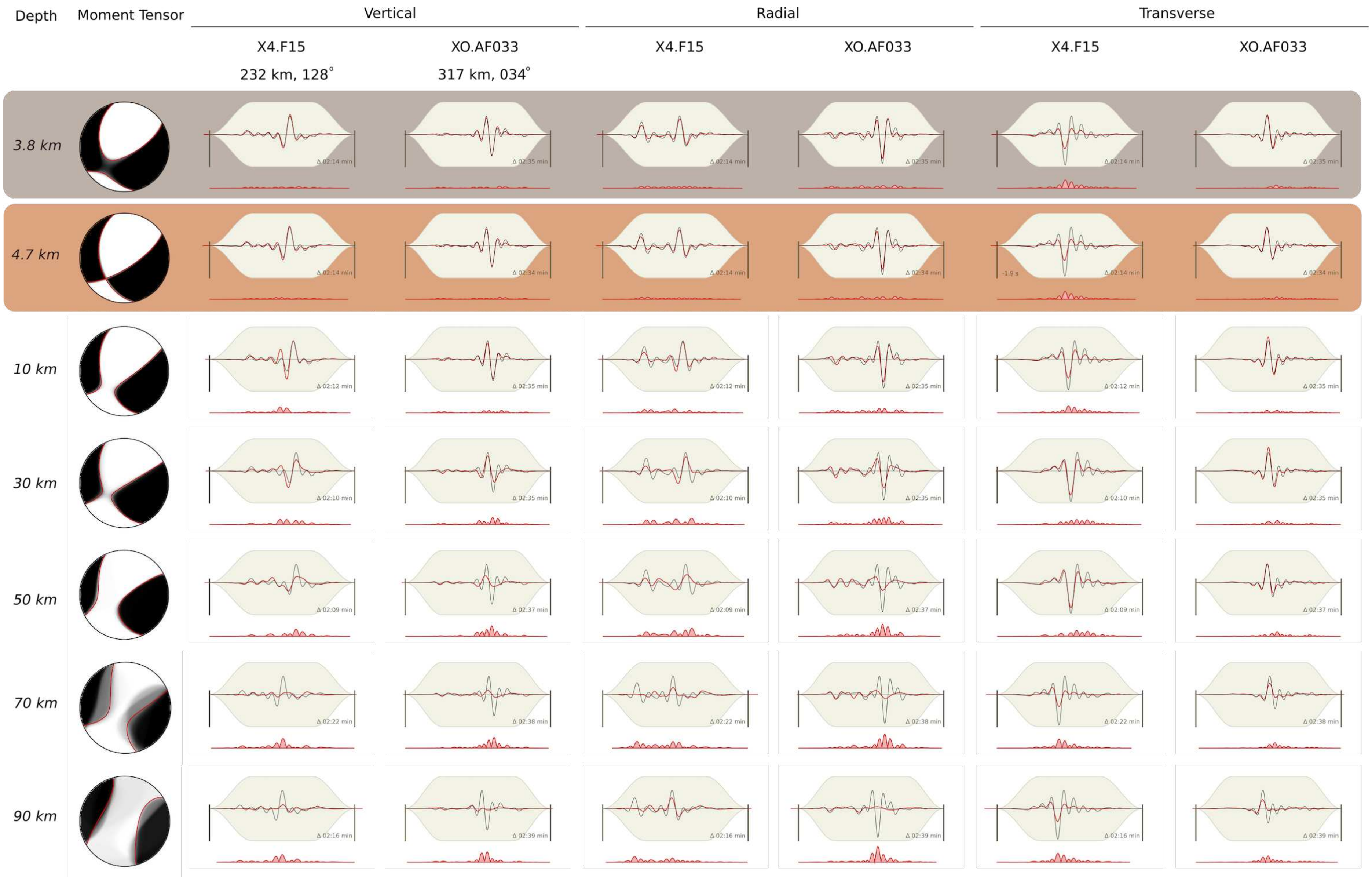


Figure 7: Regional waveform inversion results for the 2008/6/19 earthquake. Caption is as described for Figure 4.

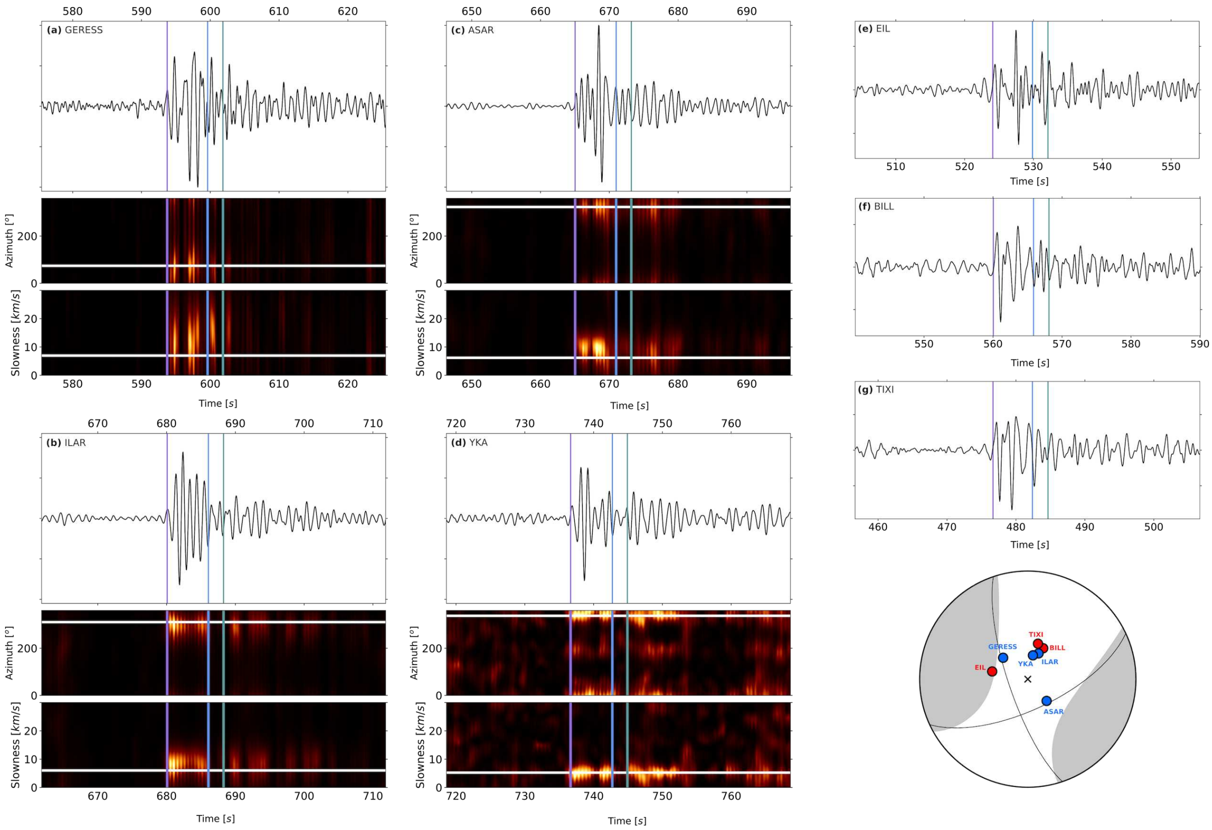


Figure 8: Array processing results for the 2008/6/19 event from arrays at (a) GERESS Array, Germany; (b) Alice Springs Array, Australia; (c) ILAR Array, Alaska, USA, (d) Yellowknife Array, Canada, and broadband waveforms from (e) EIL, Israel; (f) BILL, Russia; (g) TIXI, Russia. For each array, upper panel shows the array beam using the predicted backazimuth and slowness. Lower panels show sweeps through backazimuth and slowness space, with the colour scale indicating beam power. White horizontal lines show the predicted backazimuth and slowness. On each panel, vertical lines show *P* (purple), *pP* (blue), and *sP* (green) arrivals, using the centroid depth from the gCMT catalogue (18.3 km). Arrival time for *P* is manually re-picked. The focal mechanism shows the gCMT moment tensor and best double couple, and the pierce points of the arrays (blue) and broadband stations (red) shown.

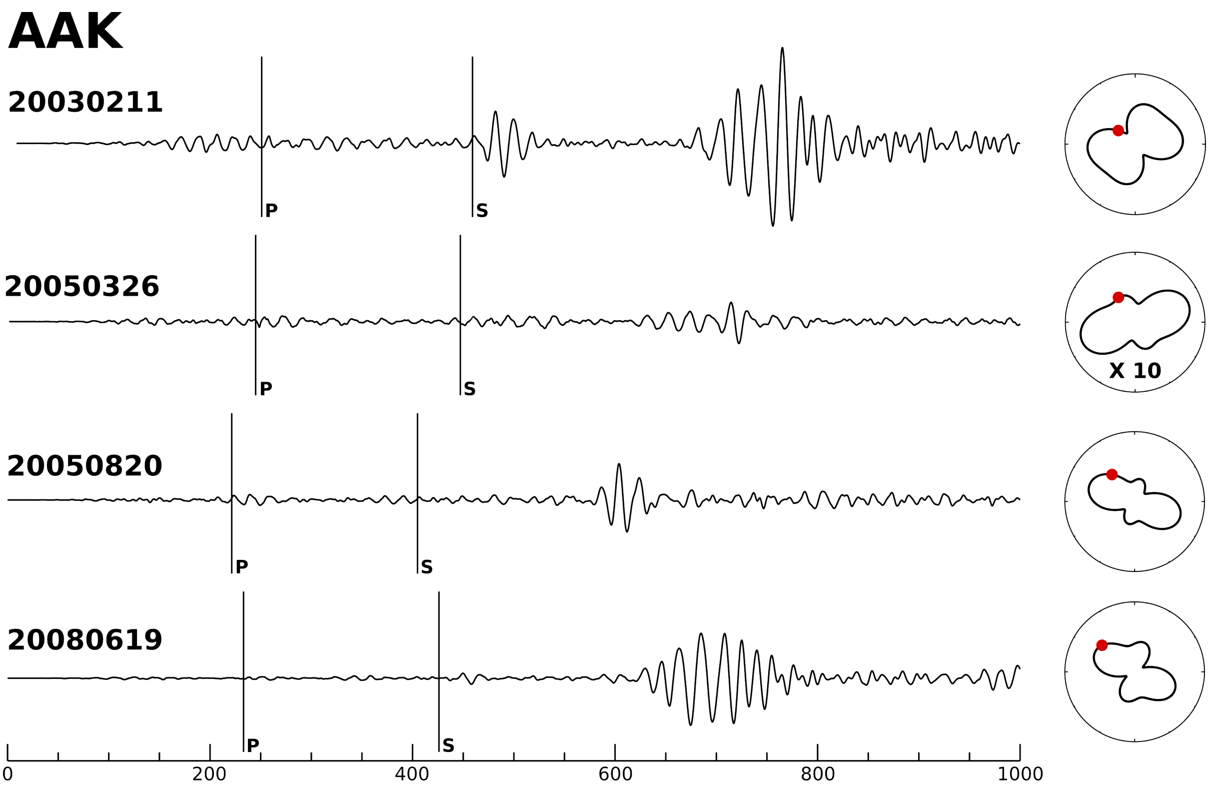


Figure 9: Rayleigh waves at the station II.AAK for all four events. Lefthand panels show vertical-component waveforms, filtered around 0.05 Hz to emphasise the 20 s fundamental mode arrivals, and with amplitudes corrected for geometrical spreading, and normalised to a common observing distance and a common source magnitude. Body wave arrivals are indicated by the labelled vertical black lines. Arrivals between 600 and 800 seconds are the Rayleigh waves. Righthand panels shown calculated Rayleigh wave radiation patterns based on our revised location and mechanism, with the red point indicating the variation of expected amplitude with azimuth at II.AAK. Note that predicted amplitudes shown for the radiation pattern for 2005/03/26 are magnified by a factor of 10 relative to those for other events, in order to be visible alongside the other radiation patterns. Results for four further stations are shown in Supplementary Figure S9–S11.

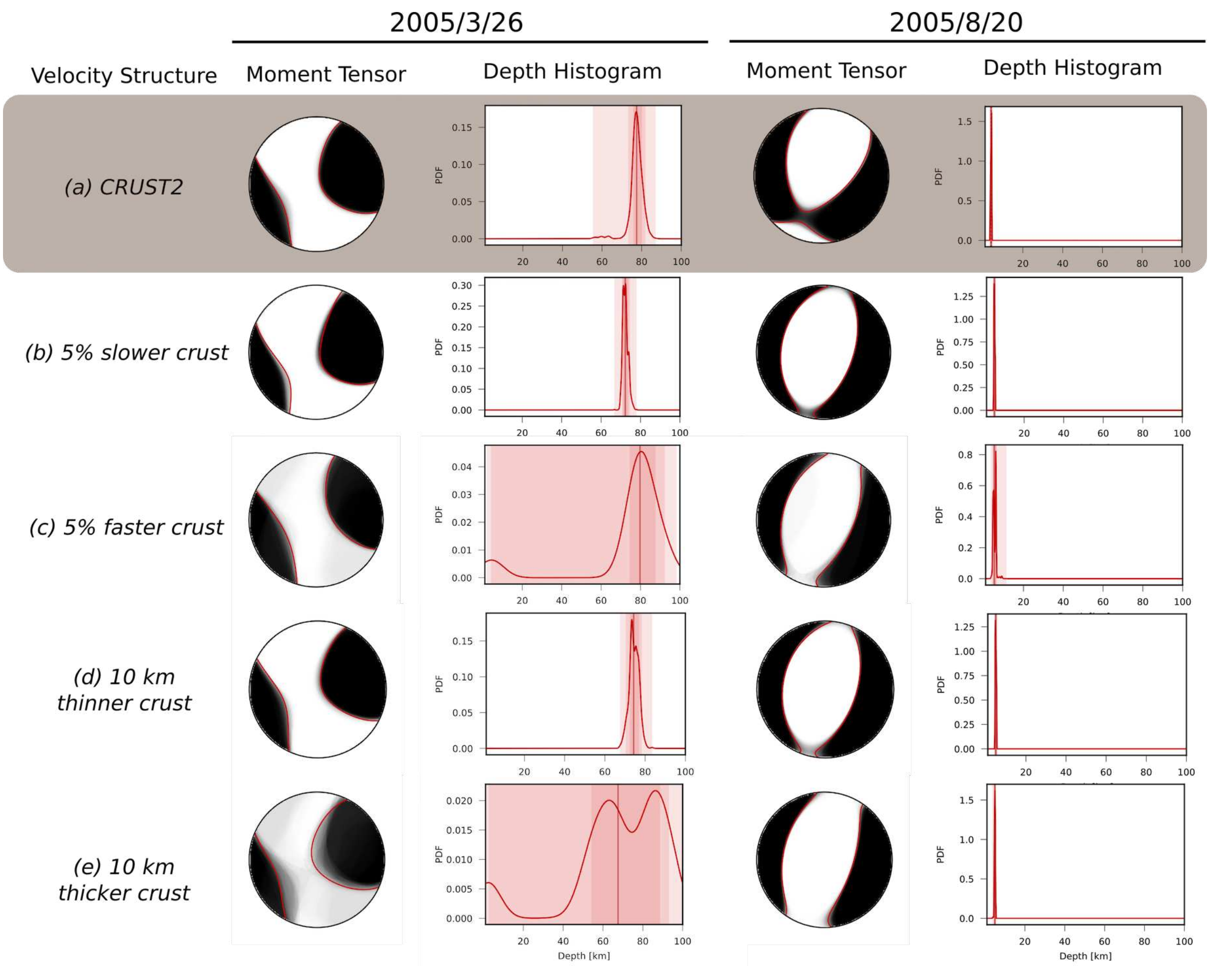


Figure 10: Tests for the impact of variations in velocity structure on regional waveform inversion results. We show probabilistic moment tensors and depth histograms for the 2005/3/26 (left) and 2005/8/20 events (right). The top row (a) shows the results for a deviatoric moment tensor using Green's functions calculated using the relevant CRUST2 velocity profile. Subsequent rows show the results obtained when recalculating the Green's functions using (b) a crustal velocity structure reduced by 5%, (c) a crustal velocity structure increased by 5%, (d) a crustal thickness where the Moho depth is reduced by 10 km, and (e) a crustal thickness where the Moho depth is increased by 10 km. As in Figures 2,4, vertical red lines show the median value of the distribution, and pink shaded areas show the 68% and 90% confident intervals, and minimum/maximum value ranges in order of decreasing intensity